A study of extragalactic planetary nebulae populations based on spectroscopy. I. Data compilation and first findings

G. Delgado-Inglada, J. García-Rojas, G. Stasińska, J. S. Rechy-García

A study of extragalactic planetary nebulae populations based on spectroscopy. I. Data compilation and first findings

G. Delgado-Inglada [ORCID],[1]⋆ J. García-Rojas [ORCID],[2,3]⋆ G. Stasińska[4] and J. S. Rechy-García[5]

[1]*Instituto de Astronomía, Universidad Nacional Autónoma de México, Apdo. Postal 70264, 04510 Ciudad de México, Mexico*
[2]*Instituto de Astrofísica de Canarias, E-38205 La Laguna, Tenerife, Spain*
[3]*Dpto. Astrofísica, Universidad de La Laguna, E-38206 La Laguna, Tenerife, Spain*
[4]*LUTH, Observatoire de Paris, PSL, CNRS, F-92190 Meudon, France*
[5]*Instituto de Radioastronomía y Astrofísica, UNAM Campus Morelia, Apartado Postal 3-72, 58090 Morelia, Michoacán, Mexico*

ABSTRACT

We compile published spectroscopic data and [O III] magnitudes of almost 500 extragalactic planetary nebulae (PNe) in 13 galaxies of various masses and morphological types. This is the first paper of a series that aims to analyse the PN populations and their progenitors in these galaxies. Although the samples are not complete or homogeneous, we obtain some first findings through the comparison of a few intensity line ratios and nebular parameters. We find that the ionized masses and the luminosities in H β, $L_{H\beta}$, of around 30 objects previously identified as PNe indicate that they are most likely compact H II regions. We find an anticorrelation between the electron densities and the ionized masses in M 31, M 33, and NGC 300 that suggests that most of the PNe observed in these galaxies are probably ionization bounded. This trend is absent in LMC and SMC suggesting that many of their PNe are density bounded. The He II λ4686/H β values found in many PNe in LMC and some in M 33 and SMC are higher than in the other galaxies. Photoionization models predict that these high values can only be reached in density bounded PNe. We also find that the brightest PNe in the sample are not necessarily the youngest since there is no correlation between electron densities and the H β luminosities. The strong correlation found between $L_{H\beta}$ and $L_{[O III]}$ implies that the so far not understood cut-off of the planetary nebula luminosity function (PNLF) based on [O III] magnitudes can be investigated using $L_{H\beta}$, a parameter much easier to study.

Key words: stars: AGB and post-AGB – stars: evolution – planetary nebulae: general – galaxies: evolution – galaxies: ISM.

1 INTRODUCTION

Planetary nebulae (PNe) are produced at the end of the lives of low- and intermediate-mass stars when the stars leave the asymptotic giant branch (AGB) after having lost most of their envelope and increase their temperatures to the point when they can ionize the surrounding gas. The PNe central stars (CSPN) eventually evolve towards the white dwarf stage, while the nebulae dissipate into the interstellar medium. The lifetimes of PNe – i.e. the time where the nebulae are visible in the optical – is dictated both by time during which the central stars are luminous and able to ionize the surrounding medium and the expansion time of the nebulae. As known, the first is extremely dependent on the initial mass of the star (Paczyński 1971; Schoenberner 1983; Vassiliadis & Wood 1993; Bloecker 1995). Recent evolution models for CSPN (Miller Bertolami 2016, with updated physical ingredients and atomic data) predict higher luminosities and much shorter evolution times than found previously. This has important consequences on our understanding of the population of PNe in galaxies (Gesicki et al. 2014; Méndez 2017; Valenzuela, Méndez & Miller Bertolami 2019).

The best way to study the evolution of PNe is to consider them in external galaxies. Of course, their large distances makes their identification subject to errors, acquirement of their spectra difficult, and makes it impossible to measure their dimensions [except in the Magellanic Clouds (MC), see e.g. Stanghellini et al. 2003]. But the fact that their distances are known (implying that their luminosities are known as well) and that their positions in the galaxies can be well determined makes their study priceless, in spite of the difficulties. The recent determinations of distances of PNe in the Milky Way using *Gaia* (Kimeswenger & Barría 2018; González-Santamaría et al. 2019; Chornay & Walton 2020; Stanghellini et al. 2020), as well as studies of PNe in the direction of the Galactic bulge (Górny et al. 2004, 2009) offer complementary approaches to the understanding of the evolution of PNe, but they are affected by other problems (difficulty to extract integrated values from the observations, strong interstellar extinction in the case of Galactic bulge PNe, etc.).

The first comparisons of PN populations in different galaxies can be traced to Webster (1976). At that time data were available only for a few PNe in the Galactic bulge and the MC. Twenty years later, Stasińska, Richer & McCall (1998) could consider four galaxies (M 31, M 32, LMC, and SMC), plus the Galactic bulge. These studies only scratched the surface of the issues worth studying. At present, the number of galaxies with spectroscopically observed PNe is much larger and allows the consideration of star formation histories of

⋆ E-mail: gdelgado@astro.unam.mx (GDI); jogarcia@iac.es (JCR)

Table 1. The galaxies considered in this paper.

(1) Name	(2) Morph type (NED)	(3) Morph type (RC3)	(4) $(B-V)_T^0$ (RC3)	(5) Distance[a] (Mpc)	(6) Distance[b] (Mpc)	(7) A_V (mag)	(8) $\log M_g$ ($M_\odot$)	(9) SFR$_{W3}$ ($M_\odot$ yr^{-1})	(10) SFR$_{W4}$ ($M_\odot$ yr^{-1})	(11) $\log$ sSFR (yr^{-1})
M 32	E2	−6	0.88	0.82	0.71	0.170	9.07	<0.01	<0.01	−11.07
NGC 4697	E2	−5	0.89	10.50	10.50	0.081	10.90	<0.01	0.04	< −11.67
NGC 205	E5 pec	−5	0.82	0.82	0.85	0.170	8.96	0.01	0.0	−10.96
NGC 147	E5 pec	−5	0.78	0.73	0.66	0.473	8.30	<0.01	<0.01	< −9.69
M 81	SA(s)ab	2	0.82	3.65	3.84	0.220	10.85	0.82	0.52	−10.94
M 31	SA(s)b	3	0.68	0.77	0.78	0.170	10.95	1.20	0.58	−10.88
M 33	SA(s)cd	6	0.47	0.86	0.94	0.114	9.61	0.45	0.33	−9.96
NGC 300	SA(s)d	7	0.58	1.93	1.81	0.035	9.41	0.11	0.08	−10.37
NGC 3109	SB(s)m[c]	9	...	1.25	1.30	0.183	8.18	<0.01	<0.0	< −9.23
LMC	SB(s)m	9	0.44	0.05	0.05	0.206	9.15	0.12	0.03	−10.07
SMC	SB(s)m pec	9	0.41	0.06	0.06	0.101	8.59	0.01	0.01	−10.59
NGC 4449	SA(s)d	10	0.41	4.11	...	0.053	7.90[d]	0.04[d]	0.12[d]	−9.30[d]
NGC 6822	IB(s)m	10	0.41	0.47	0.48	0.646	8.22	0.01	0.01	−10.22

[a]From Jarrett et al. (2019).
[b]From the PNLF papers (the references are provided in the text).
[c]Edge-on.
[d]Computed from WISE data using the procedure of Jarrett et al. (2019).

the galaxies to understand their present-day PN populations. Other related works are those by Richer (1993, 2006, 2011) and Richer & McCall (2016).

We have undertaken a compilation of published data on extragalactic PNe, to provide a general panorama for upcoming studies. Note that the objects chosen for spectroscopy are generally among the brightest, but they are not systematically the brightest ones in a given galaxy. So, care must be taken not to overinterpret the data in terms of luminosity function.

In Section 2, we explain how we selected the data and why. In Section 3, we present the observational characteristics of the compiled sample, the line strengths, and the luminosties. In Section 4, we explain how we deal with uncertainties and we evaluate them. In Section 5, we investigate whether the objects are real PNe or not. In Section 6, we study different evolutionary aspects of the PNe. Finally, our conclusions are summarized in Section 7.

2 REQUIREMENTS FOR THE SAMPLES

2.1 Galaxy selection

To construct a homogeneous set of observations, we searched in the literature for extragalactic PNe spectroscopic data fulfilling several requirements that we explain in detail in the following:

(i) We have selected galaxies with available spectroscopic data fulfilling the criteria summarized below for a minimum of five PNe.

(ii) When various sources are available for the same galaxy, we have discarded a few papers with observations of only a few PNe or with observations of worse quality than the other available sources.

(iii) The available data must allow an estimation of the reddening (generally from the observed H α/H β ratio).

(iv) Intensities (or upper limits) must be available *at least* for [O II] $\lambda3727$, He I $\lambda5876$, He II $\lambda4686$, H β, and [O III] $\lambda5007$. This choice is inspired by the work of Stasińska et al. (1998) where the authors were able to find differences between PNe in different galaxies from these few bright lines. Here, we also used other lines from the list presented in Section 2.3, when available.

(v) Since one of the objectives of this study is to understand the evolution of PNe by examining the distribution of certain line ratios

as a function of luminosity, we only use observations of objects for which photometric estimation of the H β or [O III] luminosity of the *entire* object is available, either from calibrated photometry, or from spectrophotometry in the case where the PN is entirely covered by the spectroscopic aperture.

These criteria exclude from our sample four dwarf galaxies: IC 10, NGC 185, Sextans A, and Sextans B (Magrini et al. 2005; Magrini & Gonçalves 2009; Gonçalves et al. 2012) because the number of PNe with the blue [O II] lines is less than five in all of them.

Overall, we consider data from 13 galaxies. For each galaxy, we have collected information about morphological type, mass, star formation rate, metallicity (*Z*), and distance.

We have not included PNe data in NGC 5128 from Walsh, Rejkuba & Walton (2015) because these authors reported a possible offset of the slits from the PN positions in their observations that might affect the conclusions derived from these data.

In Table 1, we present some global parameters of the considered galaxies:

(i) col. 1: the galaxy name,

(ii) col. 2: the morphological type according to NASA/IPAC Extragalactic Database (NED[1]),

(iii) col. 3: the morphological type according to the Third Reference Catalogue of Bright Galaxies (RC3; de Vaucouleurs et al. 1991),

(iv) col. 4: the total $B-V$ colour index, $(B-V)_T^0$, corrected for galactic and internal extinction, and for redshift according to RC3,

(v) col. 5: the distance, as given by Jarrett et al. (2019), taking the median of redshift-independent distances (Cepheid, tip of the red giant branch, Tully–Fisher, etc.) as tabulated in NED,

(vi) col. 6: the distance estimated in the papers that studied the planetary nebula luminosity function (PNLF) in these galaxies (Jacoby, Walker & Ciardullo 1990; Magrini et al. 2001; Méndez et al. 2001; Ciardullo et al. 2004; Corradi et al. 2005; Leisy et al. 2005; Merrett et al. 2006; Peña, Richer & Stasińska 2007a),

---

[1]The NED is funded by the National Aeronautics and Space Administration and operated by the California Institute of Technology.
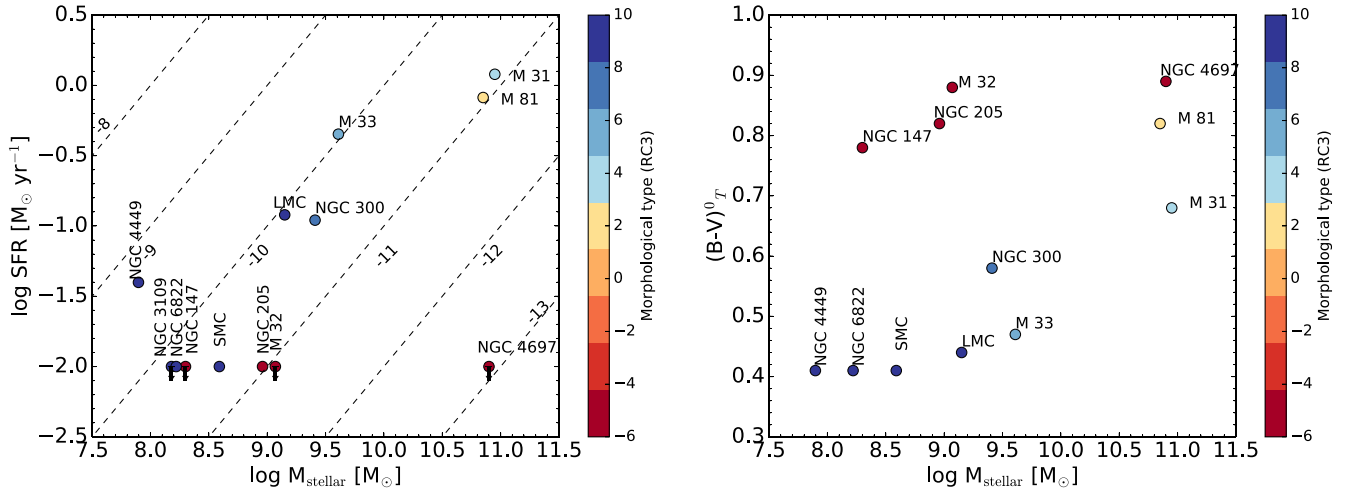
Figure 1. Star formation rate (as estimated from the W3 band) and the total $B - V$ colour index (corrected for galactic and internal extinction and for redshift) as a function of the global stellar mass of the galaxy for the considered galaxies. Values taken from Jarrett et al. (2019). In the left-hand panel, lines of constant specific star formation rate are plotted (the dashed lines). The colour bar represents the morphological type according to RC3 (de Vaucouleurs et al. 1991).

(vii) col. 7: the extinction due to the Milky Way from Schlafly & Finkbeiner (2011),

(viii) col. 8: the global stellar mass of the galaxy M_g as obtained by Jarrett et al. (2019),

(ix) col. 9: the total star formation rate as estimated by Jarrett et al. (2019) from the Wide-field Infrared Survey Explorer (WISE; Wright et al. 2010), W3 band, SFR$_{W3}$,

(x) col. 10: the total star formation rate as estimated from the WISE W4, band SFR$_{W4}$,

(xi) col. 11: the specific star formation rate as estimated by Jarrett et al. (2019).

In Fig. 1, we show some global properties of the selected galaxies. The left-hand panel shows the present star formation rate SFR$_{W3}$ as computed from the WISE W3 band, as a function of the total stellar mass of the galaxies. The dashed lines correspond to loci of equal specific star formation rates. The right-hand panel shows the $(B - V)^0_T$ colour as a function of stellar mass. The colours of the symbols indicate the de Vaucouleur types. It is thus seen that the PNe discussed in this paper belong to galaxies that cover a wide range of masses (roughly from 10^8 to $10^{11}\,\mathrm{M_\odot}$), colours, and morphological types (from very early to very late). At the high-mass end, the specific star formation rates, which can be understood as a ratio of present to past star formation rates, goes from $10^{-11.67}$ to $10^{-9.96}$. The populations of the PN progenitor masses are thus expected to be very different, being more massive for M 31, which is a galaxy that is still forming stars and less massive for NGC 4697 that mostly contains evolved stars (however, PNe in the bulge of M 31 are expected to be a population similar to that of NGC 4697). The listed specific star formation rates for M 32 and NGC 147 are upper values, but from their morphological types and galaxy colours, the progenitors of their PN population are also expected to be of low masses.

2.2 PN characterization

Most of objects appearing in the papers presenting spectroscopy of extragalactic PNe were simply taken from photometric catalogues where they were classified as PNe. The criteria that are commonly used in these catalogues to distinguish PNe from H II regions are the following: (1) the object has to be point-like, (2) it shows emission in [O III], (3) it does not show emission in the continuum (or it is very

faint), (4) the He II λ4686 line is present (this criterion is sufficient but not necessary), and (5) the [O III]/H β intensity ratio is larger than $\sim$3–4. It should be noted that low-excitation PNe, which correspond to the earliest stages of PN evolution are underrepresented because the selection generally favours objects bright in [O III].

Other criteria that are used less frequently are (1) the B and V magnitudes to confirm some ambiguous cases (Ciardullo et al. 2004, 2) the value of I([O III])/I(H α+[N II]) to estimate contamination from H II regions (Magrini et al. 2000, 3) the visual magnitudes of the central star (that are fainter for PNe than for H II regions, Peña, Stasińska & Richer 2007b), 4) the H α or H β flux that is lower in PNe than for H II regions (Peña et al. 2007b, and 5) the value of [S II]/H α intensity ratio [that it has to be lower than 0.3 to exclude supernova remnants (SNRs), Hernández-Martínez et al. 2009].

Only a few authors used the spectroscopic data to reclassify an object as a PN, an H II region, or an SNR (e.g. Peña et al. 2007b; Stasińska et al. 2013; Roth et al. 2018).

2.3 Line selection

We compiled data on a moderate subset of lines. We are mostly interested in data allowing to estimate the evolution state of the PNe and, in a future paper, in the abundances of most common elements (He, O, N, Ne, S, Ar). We also kept some lines that can serve to estimate the data quality.

The 28 lines we considered are [O II] λ3727 (in a few cases the [O II] λ3726,29 lines are resolved), [Ne III] λ3869, H I λ4102, H I λ4341, [O III] λ4363, He I λ4471, He II λ4686, [Ar IV] λ4711, [Ar IV] λ4740, H I λ4861, [O III] λ4959, [O III] λ5007, [Cl III] λ5518, [Cl III] λ5538, [N II] λ5755, He I λ5876, [O I] λ6300, [S III] λ6312, [N II] λ6548, H I λ6563, [N II] λ6584, He I λ6678, [S II] λ6716, [S II] λ6731, [Ar III] λ7136, [O II] λ7320, [O II] λ7330, and [S III] λ9069.

3 THE DATA

3.1 Description of the observing runs

Table 2 presents the observational characteristics of the compiled observing runs. In this table, we have compiled the following information:

Table 2. Summary of the considered PN observations.

Galaxy	Telescope	Instrument/ Grism	Exposure time (s)	Wavelength range (Å)	FWHM (Å)	Observing mode[a]	Aperture (arcsec)	N	Ref.[b]
M 32	3.6 m CFHT	MOS/U900	10 800	3727–4341	~3.6	MOS sl^{-1}	1.0	9	(1)
		MOS/B600	1800	3727–5876	~6.0				
		MOS/O300	900	4686–10 000	~14.0				
NGC 4697	8.2 m VLT	FORS1/300V	90 000	4450–8650	10.0	MOS sl^{-1}	1.0	14	(2)
	10 m Keck 1	LRIS-B/ 400/3400	19 800	3100–5770	2.0	MOS sl^{-1}	1.0		
NGC 205	8 m Gemini-N	GMOS/B600	7200	3600–6400		MOS sl^{-1}	1.0	8	(3)
		GMOS/R400+G5305	7200	6200–10 500	~3	MOS sl^{-1}	1.0	8	(3)
NGC 147	8 m Gemini-N	GMOS/B600+G5303	5600	3500–6500	~3	MOS sl^{-1}	1	6	(4)
		GMOS/R400+G5305	3600	6200–10 500	~8	MOS sl^{-1}	1	6	(4)
M 81 (disc)	6.5 m MMT	Hectospec	28 800	3600–9100	6.0	MOS ff^{-1}	1.5	19??	(5)
M 31 (bulge)	3.6 m CFHT	MOS/B600	8100, 1200	3727–5876	~6.0	MOS sl^{-1}	1.0	29	(1)
M 31 (bulge and disc)	4 m Kitt Peak	R-C Spec/316	23 400	3700–7400	6.9	MOS sl^{-1}	2.0	15	(6)
M 31 (outer disc)	3.5 m ARC-APO	DIS	3600–15 600	3700–9600	8.0	long-slit	1.5–2.0	16	(7)
	8 m Gemini-N	GMOS/B600	2400–7200	3600–6400	7.0	long-slit	1.5		
M 31 (outer disc)	10.4 m GTC	OSIRIS/1000B	6360–7020	3700–7850	6.3	long-slit	0.8	2	(8)
M 31 (outer regions)	10.4 m GTC	OSIRIS/1000B	7200–8100	3700–7850	6.3	long-slit	0.8	9	(9)
M 31 (substructures)	10.4 m GTC	OSIRIS/1000B	4800–9600	3700–7850	5.5	long-slit	1.0	7	(10)
M 31 (outer halo, substructures)	10.4 m GTC	OSIRIS/1000B	4800–9600	3700–7850	5.5	long-slit	1.0	10	(11)
		OSIRIS/1000R	2400–3600		6.4				
M 33 (disc, halo)	6.5 m MMT	Hectospec	14400	3600–9100	6.0	MOS ff^{-1}	1.5	96	(12)
M 33 (central region)	8.2 m Subaru	FOCAS/300B	2 × 5400	3700–6000	4.5	MOS sl^{-1}	1.2	16	(13)
		FOCAS/300R (2nd)	900, 1200	3700–5750	4.5				
		FOCAS/VPH650	2400, 3600	5300–7700	4.0				
NGC 300 (disc)	8.2 m VLT	FORS2/600B	12 600, 12 000	3600–5100	4.5	MOS sl^{-1}	1.0	26	(14)
		FORS2/600RI	11 880, 5400	5000–7500	5.0				
		FORS2/300I	7200, 1800	6500–9500	10.0				
NGC 3109	8.2 m VLT	FORS1/600B	5400, 3904	3700–5900	7.8	MOS sl^{-1}	1.7	8	(15)
		FORS1/600V	4300, 2700	4650–6800	7.8				
	6.5 m Magellan	MIKE	5400	3350–9400	0.1	Echelle	1.0		
NGC 3109	6.5 m Magellan	MIKE	900–5400	3350–9400	0.1	Echelle	1.0	8	(16)
LMC	3.58 m NTT	EMMI/3 settings	600–3600	3635–8400	2.0–11.0	long-slit	1.0–1.5	2	(17)
LMC	ESO 1.52 m	B&C	300–1800	3200–7800	3–4	long-slit	?	90[c]	(18)[d]
	MPG/ESO 2.2 m	EFOSC	300–1800	3200–7800	3–4	long-slit	?		
	ESO 3.6 m	EFOSC	300–1800	3200–7800	3–4	long-slit	?		
	3.58 m NTT	EMMI	300–1800	3200–7800	3–4	long-slit	?		
SMC	3.58 m NTT	EMMI/2 settings	600–3600	3635–7830	2.0–3.8	long-slit	1.0–1.5	1	(17)
SMC	ESO 1.52 m	B&C	300–1800	3200–7800	3–4	long-slit	?	30[c]	(18)[d]
	MPG/ESO 2.2 m	EFOSC	300–1800	3200–7800	3–4	long-slit	?		
	ESO 3.6 m	EFOSC	300–1800	3200–7800	3–4	long-slit	?		
	3.58 m NTT	EMMI	300–1800	3200–7800	3–4	long-slit	?		
SMC	3.58 m NTT	EMMI/2 settings	1200–4800	3670–7900	0.6–1.2	Echelle/long-slit	1.5	12	(19)
NGC 4449	8.4 m LBT	MODS/G400L-G670L	37800	3200–10 000	4.1–5.8	MOS sl^{-1}	1.0	5	(20)
NGC 6822	3.6 m CFHT	MOS/B600	9000	3700–6700	~7–8	MOS sl^{-1}	1.0	7	(21)
NGC 6822	8 m Gemini-S	GMOS/B600	4400	4000–6700	~2.7	MOS sl^{-1}	1.0	11	(22)
		GMOS/R600	3600	4800–7500	~1.7				
	8.2 m VLT	FORS2/600B	5400	3700–5100	4.5	MOS sl^{-1}	1.0		
		FORS2/600RI	4500	5000–7500	5.0				
	8.2 m VLT	FORS2/600B	4500	3700–5100	4.5	long-slit	1.0		
		FORS2/600RI	3000	5000–7500	5.0	long-slit			
NGC 6822	10.4 m GTC	OSIRIS/1000B	5400	3700–7850	7.5	long-slit	1.5	5	(23)

[a](MOS/sl) Multi-object Spectroscopy/Slitlets; (MOS ff^{-1}) Multi-object Spectroscopy/Fibre-fed.

[b]References: (1) Richer, Stasińska & McCall (1999); (2) Méndez et al. (2005); (3) Gonçalves et al. (2014); (4) Gonçalves et al. (2007); (5) Stanghellini et al. (2010); (6) Jacoby & Ciardullo (1999); (7) Kwitter et al. (2012); (8) Balick et al. (2013); (9) Corradi et al. (2015); (10) Fang et al. (2015); (11) Fang et al. (2018); (12) Magrini, Stanghellini & Villaver (2009); (13) Bresolin et al. (2010); (14) Stasińska et al. (2013); (15) Peña et al. (2007b); (16) Flores-Durán, Peña & Ruiz (2017); (17) Tsamis et al. (2003); (18) Leisy & Dennefeld (2006); (19) Shaw et al. (2010); (20) Annibali et al. (2017); (21) Richer & McCall (2007); (22) Hernández-Martínez et al. (2009); (23) García-Rojas et al. (2016).

[c]Some of the line intensities of these objects come from archival data.

[d]Exact wavelength coverage was not reported by Leisy & Dennefeld (2006). In this table, the reported range is the one representing the maximum coverage in their observations. The resolution is in Å pix^{-1}. Slit widths were not reported by Leisy & Dennefeld (2006).

(i) col. 1: the galaxy name (and if the PNe are located in the disc or bulge),

(ii) col. 2: the telescope,

(iii) col. 3: the instrument/mode/grism,

(iv) col. 4: the total exposure times (in s),

(v) col. 5: the covered wavelength range

(vi) col. 6: the spectral resolution full width at half-maximum (FWHM) as reported in the original references. In some cases, only the dispersion in Å pix^{-1} was reported; in these cases we estimated the spectral resolution assuming a canonical sampling of ∼3.5 pixels,

(vii) col. 7: the observing mode. The options are multi-object spectroscopy (MOS) with slitlets, MOS fibre-fed, long-slit, and echelle spectroscopy,

(viii) col. 8: the observing aperture (in arcsec). In the case of slits, we consider the slit width, in the case of fibres, we put the fibre diameter,

(ix) col. 9: *N* the number of PNe used in this work,

(x) col. 10: the reference.

As it is clearly shown in Table 2, the data have been taken either with large aperture telescopes (diameter ≥ 6 m) or with smaller telescopes but obtaining data for a significant fraction of PNe population of each galaxy. Although our aim is to have a sample of PNe spectra with a relatively homogeneous quality, we bear in mind several drawbacks that could affect the final quality of the analyzed spectra.

3.2 Line fluxes

We have decided to use the reddening-corrected intensities provided by the authors, as well as the extinction at H β derived by them. Most of the authors provided the logarithmic extinction parameter, $c(H\beta)$, that can be obtained through the comparison of the observed and theoretical (case B) line ratios of two Balmer hydrogen lines. For example, when H α and H β lines are used:

$$\frac{I_{\text{theo}}(\text{H}\alpha)}{I_{\text{theo}}(\text{H}\beta)} = \frac{I_{\text{obs}}(\text{H}\alpha)}{I_{\text{obs}}(\text{H}\beta)} \times 10^{c(\text{H}\beta)(f(\text{H}\alpha)-f(\text{H}\beta))},$$

where $f(\lambda)$ is the adopted reddening law (e.g. Cardelli, Clayton & Mathis 1989). In a few cases, we have derived the value of $c(H\beta)$ from the $E(B-V)$ given by the authors (Richer et al. 1999; Richer & McCall 2007; Annibali et al. 2017). The relation between these two quantities depends on the form of the extinction curve: $c(H\beta) = 0.4R_V E(B-V)$. We have used the same R_V values as those adopted by the authors.

This is not a fully consistent approach, since the procedures for dereddening vary, depending on the instrumental set-up, on the quality of data (e.g. whether the H γ and H δ intensities can be used with confidence) and on the adopted reddening law. But we did not see any advantage of recomputing the reddening, since in the wavelength range we are considering, the reddening laws adopted by the different authors are equivalent. There are two cases where we have computed the extinction coefficient and corrected the observed lines because the uncertainties in the reddening-corrected intensities were not provided by the authors: the PNe from Stanghellini et al. (2010) for M 81 and the PNe from Magrini & Gonçalves (2009) for M 33. In both cases, we have adopted $R_V = 3.1$ and the extinction law by Cardelli et al. (1989).

The sky subtraction is a critical step when dealing with extragalactic PNe spectra. The accuracy of this subtraction relies on the observing technique as well as on the characteristics of each galaxy. Data obtained with fibres are the least reliable since the 'sky' spectra is taken far from the PN loci. Note that, in our compilation, only the data from Stanghellini et al. (2010) and Magrini & Gonçalves (2009) for M 81 and M 33 were obtained with fibres. Data obtained from long-slit or MOS/slitlets observations are more reliable if the sky is measured on both sides of the object. However, the 'sky' emission, which actually is dominated by the light from stellar populations encompassed by the observing aperture, may be far from uniform. As an example of the complexity of sky subtraction we refer to the case of PN 29 in the bulge of M 31; for this PN, Jacoby & Ciardullo (1999) and Richer et al. (1999) obtained very different line intensities. Using integral field unit (IFU) observations, Roth et al. (2004) showed that indeed the 'sky' emission around PN 29 was not uniform. These authors pointed out the importance of a proper knowledge of the contribution of the continuum light of unresolved stars with a small angular separation from the target or from emission-line spectra of H II regions and diffuse nebulosities of the interstellar medium to the observed spectra of point-like sources, and demonstrated that this contribution can be reasonably well determined with IFU spectroscopy when using full 2D spatial information and point-spread function fitting techniques. Unfortunately, among the data collected for our paper, only those from Roth et al. (2004) allow such a treatment, and the number of PNe in that paper that comply the requirements presented in Section 2.1 is not sufficient. Another option would be to estimate the stellar contribution directly from the *stellar* lines present in the spectrum of the object, as done for example by Kreckel et al. (2017) for PNe in the galaxy NGC 628 that were observed with the Multi-unit Spectroscopic Explorer (MUSE; Bacon et al. 2010). Sadly, the wavelength range of MUSE is restricted to $\lambda > 4650$ Å, so these data do not appear in our compilation. There is no doubt that the advent of similar instruments but working at shorter wavelengths, such as BlueMUSE (Richard et al. 2019), will allow considerable progress in spectroscopic studies of extragalactic PNe. For the time being, we have to live with what is available, and remember that some caution should be taken when interpreting the results obtained from the emission-line spectra of extragalactic PNe, especially in regions containing old stellar populations.

Taking into account the relatively low resolution of the majority of the spectra in the sample, and that we are interested in the density diagnostic [Ar IV] λ4740/[Ar IV] λ4711, we have carefully corrected the [Ar IV] λ4711 emission line from the contribution of He I λ4713 emission. To do this, we used the theoretical He I λ4713/He I λ5876 ratio for $n_e = 10^3$ cm^{-3} and T_e([O III]) derived from the spectra (or $T_e = 10^4$ K in case the auroral [O III] λ4363 is not detected in the spectra). We consider this a sufficiently good approach given the small dependency of the He I λ4713/He I λ5876 intensity ratio with n_e (less than 10 per cent in the 10^3-10^5 cm^{-3} density range). We have performed this correction in the spectra of the PNe of the following galaxies: M 31 (Kwitter et al. 2012; Balick et al. 2013; Corradi et al. 2015), M 33 (Magrini & Gonçalves 2009; Bresolin et al. 2010), NGC 300 (Stasińska et al. 2013), NGC 3109 (Peña et al. 2007b), LMC (Leisy & Dennefeld 2006), SMC (Leisy & Dennefeld 2006; Shaw et al. 2010), NGC 4449 (Annibali et al. 2017), and NGC 6822 (Richer & McCall 2007; Hernández-Martínez et al. 2009); all these spectra have a spectral resolution greater than 2–3 Å and a detected line at ∼4711 Å. A more detailed discussion on this correction has been done in Section 5.

Lines of [O II] λλ3726+29 are summed in the tables even if observations allow one to separate the lines. The only PNe where this doublet is resolved are: one object in NGC 3109 observed by Peña et al. (2007b) and the sample studied by Flores-Durán et al. (2017), the PNe in the LMC and SMC reported by Tsamis et al. (2003), and the SMC sample observed by Shaw et al. (2010).

3.3 Luminosities

When available, the [O III] luminosity was computed from photometry, using the [O III] λ5007 magnitudes, m(5007), and the formula from Jacoby (1989) to convert them into fluxes. This is especially important for PNe in the MC, which are larger than the observing slits. For the MC, we thus use only the data for which the magnitude m(5007) is given in Jacoby et al. (1990).

For the other galaxies, if the [O III] λ5007 magnitude was not provided in the papers listed in Table 2 we have compiled them from Ciardullo et al. (1989), Merrett et al. (2006) for M 31, Ciardullo et al. (1989) for M 32, Ciardullo et al. (2004) for M 33, Magrini et al. (2001) for M 81, Corradi et al. (2005) for NGC 147 and NGC 205, Peña et al. (2012), Roth et al. (2018) for NGC 300, Peña et al. (2007a) for NGC 3109, Méndez et al. (2001) for NGC 4697, and Leisy et al. (2005) for NGC 6822.

If no photometry is available, we directly used the measured fluxes from spectrophotometric data. This is the case for the PNe in NGC 4449.

The values of m(5007) for PNe in M 81 as provided by Magrini et al. (2001) were corrected for the interstellar extinction by only considering the foreground Galactic extinction towards M 81. We uncorrected the magnitudes using the values of A_V and $E(B - V)$ given by Magrini et al. (2001) and then computed the [O III] and H β luminosities in the same way as for the other PNe, i.e. using the extinction coefficients and line ratios obtained from spectrophotometric data given by Stanghellini et al. (2010).

It is worth mentioning that in NGC 300 Roth et al. (2018) found a systematic offset with a median of ∼0.67 mag between their computed magnitudes from deep MUSE data and those derived by Peña et al. (2012) for the PNe in common, being the value of m(5007) from Peña et al. (2012) higher than those computed by Roth et al. (2018). These differences can be due to problems in flux calibration and/or slit losses and translates into differences of a factor of 2 in the fluxes obtained by both authors. Roth et al. (2018) found a much better agreement with the magnitudes reported by Soffner et al. (1996) for PNe in common. We have used the magnitudes from Roth et al. (2018) when available and corrected the magnitudes from Peña et al. (2012) by 0.67 mag otherwise.

4 DEALING WITH UNCERTAINTIES AND UPPER LIMITS

4.1 Determination of the uncertainties in line strengths

In principle, determining uncertainties in extinction-corrected line strengths requires to start from raw, flux-calibrated data, estimate the extinction with its errors bars, then compute the uncertainties in extinction-corrected line fluxes. The data available in most of the references we used do not allow such a procedure.

We have followed slightly different approaches, depending on the information given in the original data source and on the availability of similar observations for a given galaxy.

If error bars are specified explicitly in the original source, we simply adopt them. This is the case for the PNe taken from Richer et al. (1999), Gonçalves et al. (2007), Richer & McCall (2007), Hernández-Martínez et al. (2009), Magrini & Gonçalves (2009), Stanghellini et al. (2010), Stasińska et al. (2013), García-Rojas et al. (2016), Annibali et al. (2017), and Flores-Durán et al. (2017).

Sometimes no error is given for the H β intensity, so we have estimated it from a logarithm linear fit between the relative uncertainties versus the line intensities of the other lines. The PN samples

for which we have to do this are those from Bresolin et al. (2010), Kwitter et al. (2012), Balick et al. (2013), Fang et al. (2015), and Fang et al. (2018).

For PNe data of LMC and SMC from Tsamis et al. (2003) and Shaw et al. (2010), the authors assigned percentage uncertainties depending on the brightness of the lines. In this case we have attributed errors using a formula to reproduce the assigned uncertainties. For Tsamis et al. (2003) the formula is $\Delta I/I \sim 0.05/[I(\lambda)/I(H\beta)]^{0.4}$, and for Shaw et al. (2010) it is $\Delta I/I \sim 0.08/[I(\lambda)/I(H\beta)]^{0.3}$. As for the PNe from Leisy & Dennefeld (2006), these authors reported that the uncertainty of lines with intensities between 1–5 per cent I(H β) scales approximately with the inverse square root of their intensity ratio to H β. Accordingly, we decided to use the following formula to compute uncertainties: $\Delta I/I \sim 0.08/[I(\lambda)/I(H\beta)]^{0.3}$. Whenever possible, we checked the error bars attributed by us to the observations by looking at the published spectra. This of course is a very rough estimation, since for a given observing run the uncertainties depend on the line fluxes (and not on the ratio of the line flux with H β), on the wavelength (blue is always noisiest), and on the exposure time. Additionally, they should be estimated on observed data (not dereddened) but this makes little difference.

The papers by Corradi et al. (2015), Jacoby & Ciardullo (1999), and Méndez et al. (2005) do not provide uncertainties at all. For the M 31 PNe studied by Corradi et al. (2015), we have applied a logarithmic linear fit to the relative uncertainties versus the flux of the line for the objects reported by Balick et al. (2013) and Kwitter et al. (2012). We took advantage of the fact that both observations were made with the same telescope+instrument (OSIRIS+GTC) and similar configurations. Then, we used the fit to estimate the uncertainties associated with the line fluxes reported by Corradi et al. (2015). The M 31 PNe studied by Jacoby & Ciardullo (1999) were observed with a different telescope and configuration than any other sample considered in this paper. Therefore, we decided to perform a similar analysis to that carried out for the data from Corradi et al. (2015). For the observations reported by Méndez et al. (2005) in NGC 4697, we used the uncertainties reported by Stasińska et al. (2013) for PNe in NGC 300 and a similar approach to the one that was used for M 31. Both authors used similar telescope and instrumentation: FORS1/VLT MOS with grism 300V by Méndez et al. (2005) and FORS2/VLT MOS with grisms 600B, 600RI, and 300I by Stasińska et al. (2013).

As for NGC 3109, Peña et al. (2007b) provide relative uncertainties for a few ranges in the values of the line intensities. However, we decided to apply the same procedure as described above to derive the uncertainties for all the lines using the uncertainties reported by Stasińska et al. (2013) for PNe in NGC 300 since the observations have similar characteristics in both galaxies.

Fig. 2 shows one example of the fits we have performed to estimate the uncertainties in the cases where the authors do not provide them.

The uncertainties in line ratios that are used later in the text, such as [O III]/H β, for example, have been estimated from the uncertainties in [O III] and H β fluxes, propagated analytically, assuming the errors to be independent for simplicity.

Note that neglecting the uncertainty in the reddening correction has only a minor impact in optical line ratios, since most of our objects have a value of c(H β) much smaller than 1 (see Fig. 12). The line ratio with the strongest impact is that of [O II] λ3727/H β, for which we estimate a possible error of about 25 per cent in the worst cases (i.e. when the relative uncertainties in H α and H β lines are ∼30 per cent and c(H β) is of the order of 1, which occurs only in a small minority of cases).
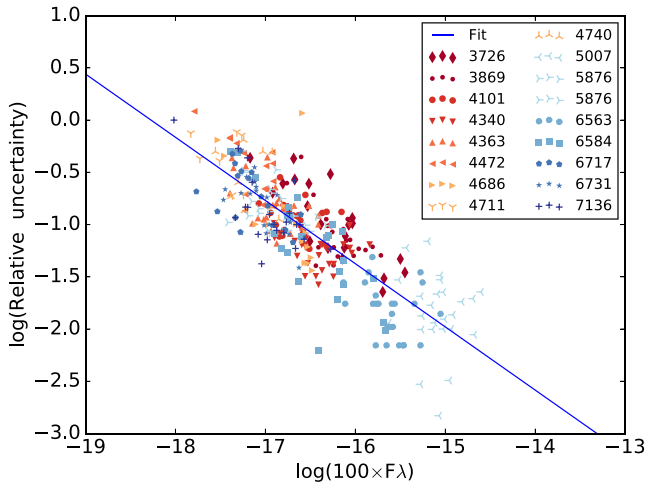
Figure 2. Values of the relative uncertainties as a function of the line intensities weighted by the total Hβ flux for different lines taken from Stasińska et al. (2013). The solid line represents our fit.

4.2 Upper limits

In general, we consider upper limits as stated in the original papers. If upper limits of any of the necessary lines ([O II] $\lambda 3727$, [O III] $\lambda 5007$, He I $\lambda 5876$, and He II $\lambda 4686$) have not been reported in the original references, we have adopted as an upper limit the uncertainty of the faintest line reported in the same wavelength range.

4.3 Graphical evaluation of uncertainties

Figures appearing hereafter are presented as 'small multiple diagrams' according to the denomination of Tufte (1990) to give a panoramic view of our sample. In case one is interested in details, the figures can be enhanced, since they are published at full resolution.

In Figs 3–5, we present the following three plots for all the galaxies: (i) the [N II] $\lambda 6584/\lambda 6548$ ratio as a function of [N II]$\lambda 6584/$Hβ $\times F_{H\beta}$, (ii) the [O III] $\lambda 5007/\lambda 4949$ ratio as a function of [O III] $\lambda 5007/$H$\beta \times F_{H\beta}$, and (iii) the H$\gamma/$Hβ ratio as a function of $F_{H\beta}$. These plots allow us to have an idea of the quality of the observational data. The number that appears at the top left corner of each panel indicates the number of PNe plotted in each panel. The upper panels correspond to early-type galaxies (M 32, NGC 4697, NGC 205, and NGC 147), the middle panels to spiral galaxies (M 81, M 31, M 33, and NGC 300, and NGC 3109), and the lower panel to the irregular galaxies (LMC, SMC, NGC 4449, and NGC 6822). We have skipped plotting PNe with upper limits in the line intensities as they are not useful for a quality check. In each of these three figures, we also show (upper right corner) the weighted standard deviation of the values of [O III] $\lambda 4959/\lambda 5007$, [N II] $\lambda 6548/\lambda 6584$, and H$\gamma/H\beta$ divided by the theoretical value. This quantity provide a more quantitative comparison between galaxies.

We have computed the error bars in the following plots through analytical error propagation. We have only considered the available uncertainties in the quantities involved in the calculations (i.e. basically those related to the uncertainties in line fluxes).

To distinguish between the various references we have used a colour- and symbol-code, of course better seen when zooming on the figures. The colour and symbol code are defined at the top right corner of each figure. The number scheme for each galaxy is as follows:

(i) M 31: (1) Balick et al. (2013, B13), (2) Corradi et al. (2015, C15), (3) Fang et al. (2015, F15), (4) Fang et al. (2018, F18), (5) Jacoby & Ciardullo (1999, J99), (6) Kwitter et al. (2012, K12), (7) Richer et al. (1999, R99).

(ii) M 33: (1) Magrini & Gonçalves (2009, M09), (2) Bresolin et al. (2010, B10).

(iii) NGC 3109: (1) Flores-Durán et al. (2017, FD17), (2) Peña et al. (2007b, P07).

(iv) LMC: (1) Leisy & Dennefeld (2006, LD06), (2) Tsamis et al. (2003, T03).

(v) SMC: (1) Leisy & Dennefeld (2006, LD06), (2) Shaw et al. (2010, S10), (3) Tsamis et al. (2003, T03).

(vi) NGC 6822: (1) García-Rojas et al. (2016, GR16), (2) Hernández-Martínez et al. (2009, HM09), (3) Richer & McCall (2007, R07).

Departures of the [O III] $\lambda 4959/\lambda 5007$ ratios from the theoretical value that strongly exceed the error bars indicate that the estimated error bars are too small. This concerns especially some objects in M 33 from the observations of Magrini & Gonçalves (2009).

The error bars on the [N II] $\lambda 6548/\lambda 6584$ ratios are larger than those on the [O III] $\lambda 4959/\lambda 5007$ ratios because these lines are in general weaker than the [O III] lines and because of the difficulty of deconvolving [N II] $\lambda 6548$ from Hα, especially for high-excitation objects observed with low spectral resolution. We note that large error bars on the [O III] $\lambda 4959/\lambda 5007$ ratios at low fluxes, especially in M 31, M 33, LMC, and SMC indicate that the estimations of the error bars in this case must have been too conservative, since most of the nominal values of this ratio fall close to the theoretical value.

Another way to appreciate differences between galaxies is to look at the values of the weighted standard deviation of these ratios divided by their theoretical values. This quantity is significantly higher in the case of [N II] $\lambda 6548/\lambda 6584$ than in that of [O III] $\lambda 4959/\lambda 5007$, as expected. The two exceptions are NGC 205 and NGC 147 with a similar value in both cases. The worst cases are M 31, M 33, LMC, NGC 3109, NGC 4449, and NGC 6822 in Fig. 3 and M 33, M 81, and NGC 3109 in Fig. 4. Note that many of the galaxies have a few outliers in Fig. 3. They should be considered with caution in the forthcoming papers.

Note that data from Bresolin et al. (2010) for M 33 PNe are not reported in the plots of [O III] $\lambda 4959/\lambda 5007$ and [N II] $\lambda 6548/\lambda 6584$ because the weakest lines of these doublets are not listed in the original paper, but as can be judged from the spectra shown in that paper, the data are of excellent quality.

For the H$\gamma/$Hβ ratio, departures from the theoretical value exceeding the error bars may indicate an underestimation of the error bar in the Hγ emission line intensity, a problem in the spectral calibration over a wavelength range of about 500 Å, or the fact that the determination of the stellar continuum in the region of Hγ does not take into account stellar absorption with sufficient accuracy; however, this possibility is unlikely in most of the objects in our sample and should only be considered in galaxies with important old stellar populations or in the bulge of spiral galaxies like M 31. The H$\gamma/$Hβ line ratio reported in the figure is in agreement with the theoretically expected value for some of the galaxies: M 31, NGC 300, NGC 3109, LMC, SMC, either because the reddening was obtained using these lines precisely or because the observers paid special attention to it. But it is very far from it in NGC 205, M 32, M 81, and many objects in M 33. The first five galaxies have a value of the weighted standard deviation of H$\gamma/$Hβ divided by its theoretical value $\lesssim 0.01$ while this value is $\gtrsim 0.03$ for NGC 205, M 32, M 81, and M 33. Whatever the cause, an incorrect H$\gamma/$Hβ ratio implies an incorrect [O III]
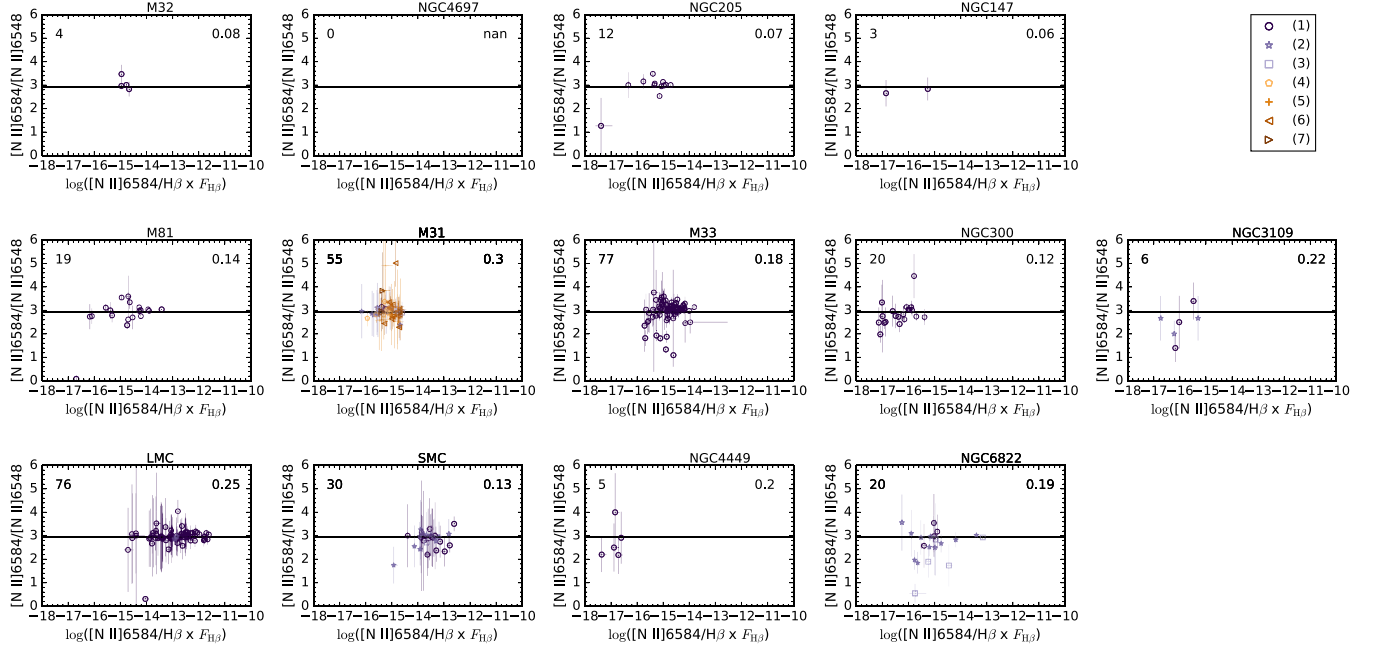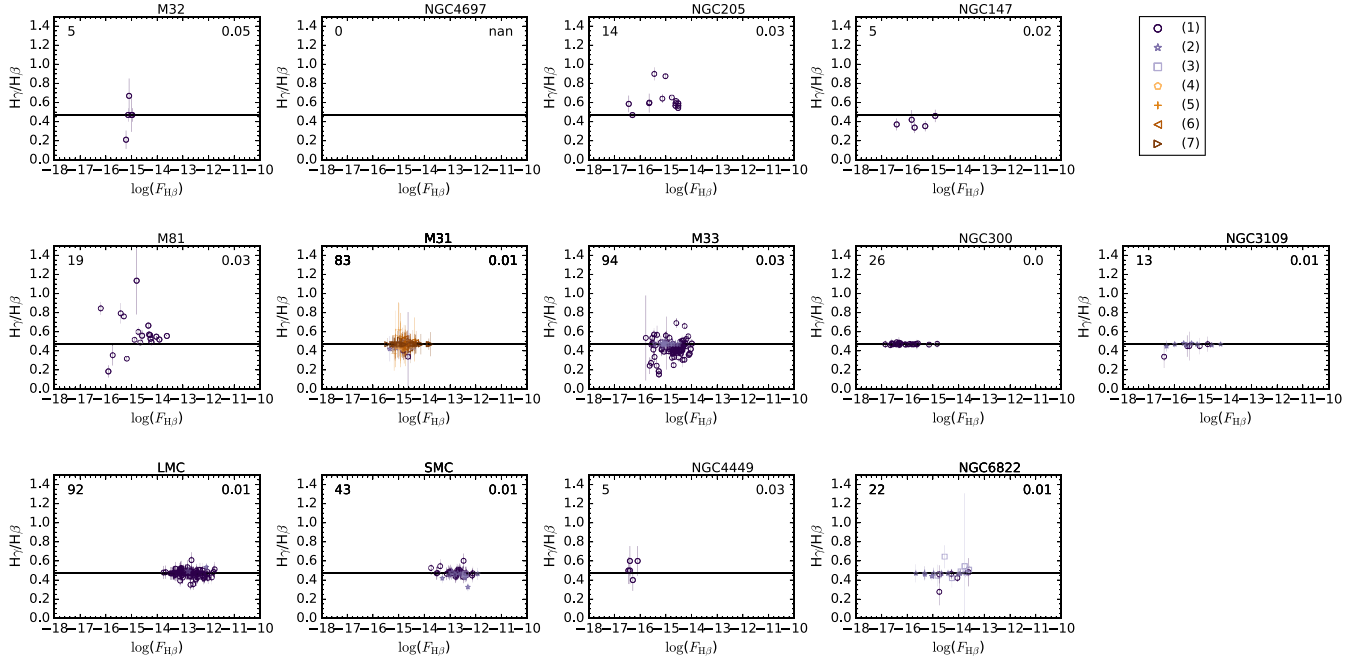
Figure 3. Assessment of accuracies in line fluxes. Values of [N II] $\lambda 6584/\lambda 6548$ ratio as a function of [N II] $\lambda 6584/H\beta \times F_{H\beta}$. Upper panels: early-type galaxies, middle panels: spiral galaxies, lower panels: irregular galaxies. The number that appears at the top left corner of each panel indicates the number of PNe plotted in the panel. The number that appears at the top right corner of each panel indicates the weighted standard deviation of the [N II] $\lambda 6584/\lambda 6548$ values divided by its theoretical value. The colour and symbol code for the galaxies with more than one reference is based on the following numbering: M 31: (1) B13, (2) C15, (3) F15, (4) F18, (5) J99, (6) K12, (7) R99. M 33: (1) M09, (2) B10. NGC 3109: (1) FD17, (2) P07, LMC: (1) LD06, (2) T03. SMC: (1) LD06, (2) S10, (3) T03. NGC 6822: (1) GR16, (2) HM09, (3) R07.
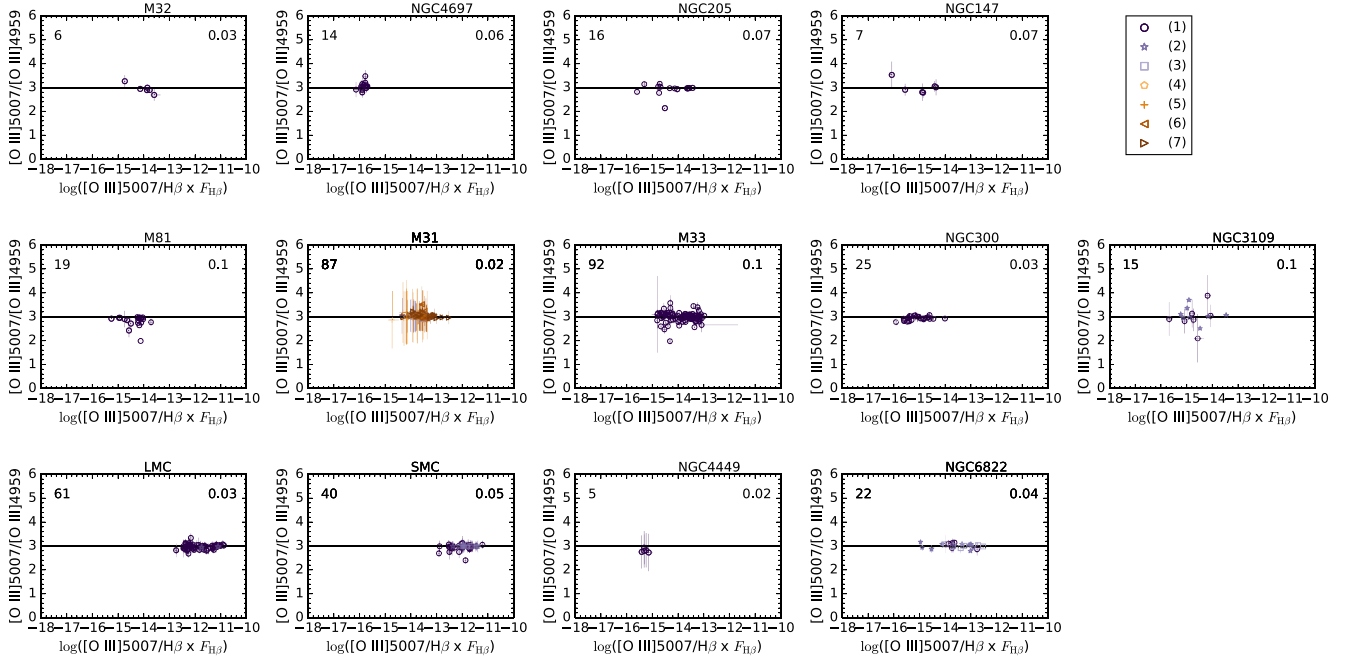
Figure 4. Assessment of accuracies in line fluxes. Values of [O III] $\lambda 5007/\lambda 4949$ ratio as a function of [O III] $\lambda 5007/H\beta \times F_{H\beta}$. Upper panels: early-type galaxies, middle panels: spiral galaxies, lower panels: irregular galaxies. The number that appears at the top left corner of each panel indicates the number of PNe plotted in the panel. The number that appears at the top right corner of each panel indicates the weighted standard deviation of the [O III] $\lambda 5007/\lambda 4949$ values divided by its theoretical value. The numbering of the references is the same as in Fig. 3.

Figure 5. Assessment of accuracies in line fluxes. Values of Hγ/Hβ as a function of $F_{H\beta}$. Upper panels: early-type galaxies, middle panels: spiral galaxies, lower panels: irregular galaxies. The number that appears at the top left corner of each panel indicates the number of PNe plotted in the panel. The number that appears at the top right corner of each panel indicates the weighted standard deviation of the Hγ/Hβ values divided by its theoretical value. The numbering of the references is the same as in Fig. 3.

Table 3. Atomic data set used for collisionally excited lines and recombination lines.

	Collisionally excited lines	
Ion	Transition probabilities	Collision strengths
O^{2+}	Froese Fischer & Tachiev (2004), Storey & Zeippen (2000)	Storey, Sochi & Badnell (2014)
S^+	Mendoza & Zeippen (1982)	Tayal & Zatsarinny (2010)
Ar^{3+}	Mendoza & Zeippen (1982)	Ramsbottom & Bell (1997)
	Recombination lines	
Ion	Effective recombination coefficients	
H^+	Storey & Hummer (1995)	
He^+	Porter et al. (2012, 2013)	

$\lambda 4363/\lambda 5007$ ratio by about the same amount, which will affect the determination of the electron temperature.

5 THE REAL NATURE OF THE NEBULAE IN OUR SAMPLES

In this section, we examine whether the studied objects, which are considered as PNe in the original papers,[2] could be something else such as giant H II regions in late-type galaxies, or SNRs in all types.

We also try to get a hint on the behaviour of the density: are the densities derived by [Ar IV] and [S II] systematically different? In case only one of the two is available, can it be used as representative of the whole nebula for nebular mass estimations and for abundance ratios calculations?

---

[2]For NGC 3109, we have removed from our tables PN7, following the arguments presented by Peña et al. (2007b). Similarly, for NGC 300, we included object 74 and discarded object 39 following the strong arguments presented by Stasińska et al. (2013).

Fig. 6 shows the values of n_e[S II] $\lambda 6731/\lambda 6717$ as a function of n_e[Ar IV] $\lambda 4740/\lambda 4711$. Both values were derived with PYNEB v.1.1.1 (Luridiana, Morisset & Shaw 2015). The number that appears at the top left corner of each panel indicates the number of objects plotted in the panel (upper limits or objects that do not have a value of the two parameters plotted are not counted, but these objects are represented in the plots at a value of density equal to 10 cm^3). As in the previous figures, the upper panels correspond to early-type galaxies, the middle panels to spiral galaxies, and the lower panels to the irregular galaxies. The colour and symbol code for the references is the same as in previous figures. The atomic data we have adopted to compute the densities, as well as the correction for the [Ar IV] $\lambda 4711$ line are shown in Table 3.

In some cases, there are two determinations for the densities, through [S II] and [Ar IV]. In most cases, there is only one determination, and in some cases no determination at all. Most of our objects have densities between 1000 and 10 000 cm^{-3}. When both n_e[S II] and n_e[Ar IV] are available, the density derived from [Ar IV] tends to be larger, typically by a factor of $\sim$10 but sometimes by up to a factor of $\sim$200. We have checked the effect of self-absorption in the two He I lines we used to compute the theoretical ratio to correct the [Ar IV] $\lambda 4711$ line, He I $\lambda 4713$ and $\lambda 5876$, but this ratio would be affected in the opposite direction, i.e. if the effect is not considered in the correction, we would have lower densities.

The relation between n_e[S II] and n_e[Ar IV] that we see in Fig. 6 could be due to the density structure of the objects, with the density decreasing outwards. But this seems in contradiction with the recent finding by Rodríguez (2020) that in Galactic PNe those two densities are similar. However, one must recall that in the case of Galactic PNe, most of the times the observing aperture covers only a small portion of the object – generally chosen to be the brightest –, so the density measurements in Galactic and extragalactic PNe do not exactly mean the same. This subject needs to be investigated further,
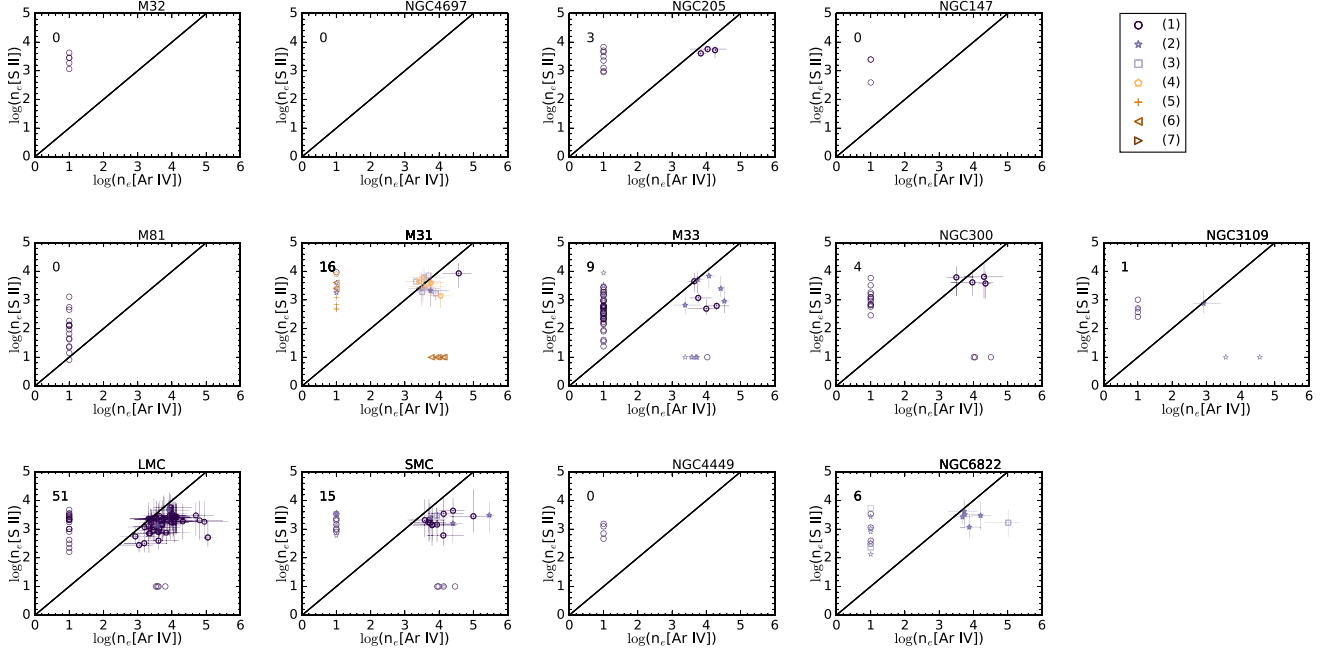
Figure 6. Values of n_e[S II] λ6731/λ6717 as a function of n_e[Ar IV] λ4740/λ4711. Upper panels: early-type galaxies, middle panels: spiral galaxies, lower panels: irregular galaxies. The number that appears at the top left corner of each panel indicates the number of PNe plotted in each panel. When densities for a given line-ratio were not available, they were systematically put to 10. The numbering of the references is the same as in Fig. 3.
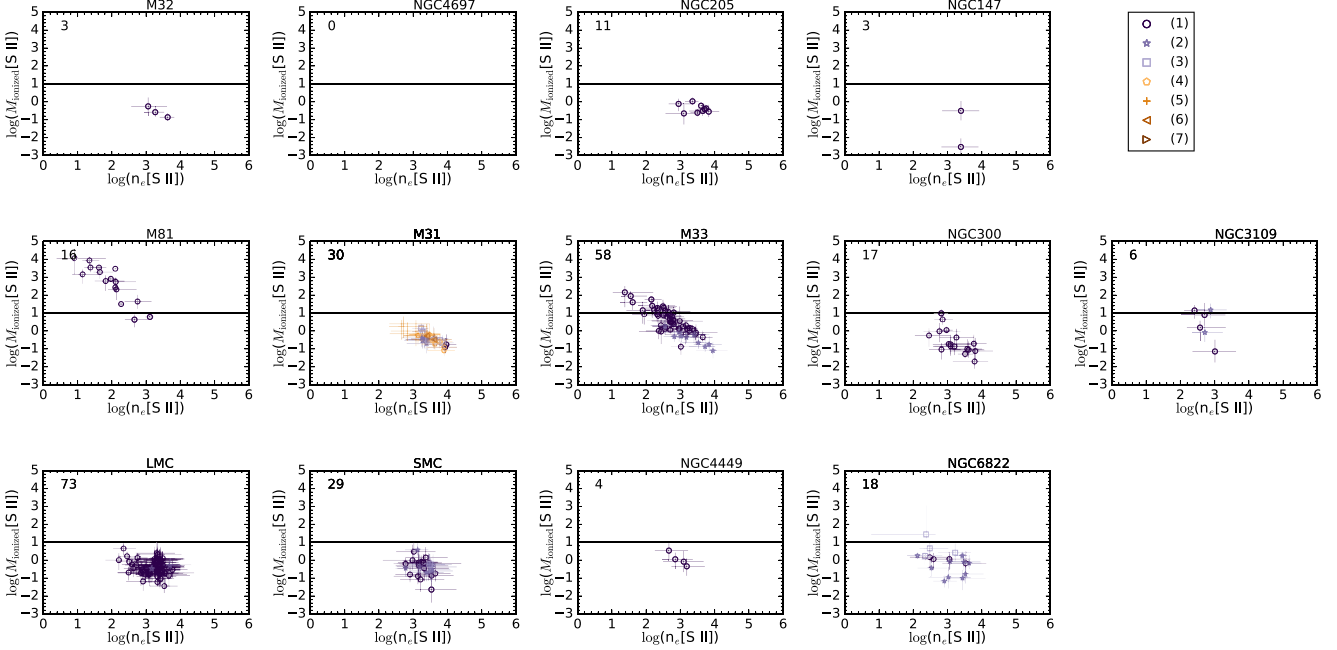
Figure 7. Values of the ionized mass as a function of the electron density derived both from [S II] lines. Upper panels: early-type galaxies, middle panels: spiral galaxies, lower panels: irregular galaxies. The number that appears at the top left corner of each panel indicates the number of PNe plotted in each panel. The numbering of the references is the same as in Fig. 3.

as the value adopted for the electron densities in the calculation of nebular masses or of some abundance ratios is important.

Figs 7 and 8 show the values of the ionized mass as a function of the electron density derived from [S II] and [Ar IV] lines, respectively. The ionized masses have been derived from the equation given by Stasińska et al. (2013):

$$M_{\text{ionized}} = 37.5 L(\text{H}\beta)/n_e, \quad (1)$$

where $L(\text{H}\beta)$ and M_{ionized} are in solar units, and n_e is the mass-weighted average electron density in cm^{-3}. In practice, we use the [S II] or [Ar IV] ratios to estimate this density.

Since we do not know which of n_e[S II] or n_e[Ar IV] better represents the bulk density of the ionized gas, we estimated the masses of the ionized gasses using both densities in turn.

In PNe, the ionized masses cannot be larger than a few solar masses at the very most, since PNe arise from intermediate-mass stars. The
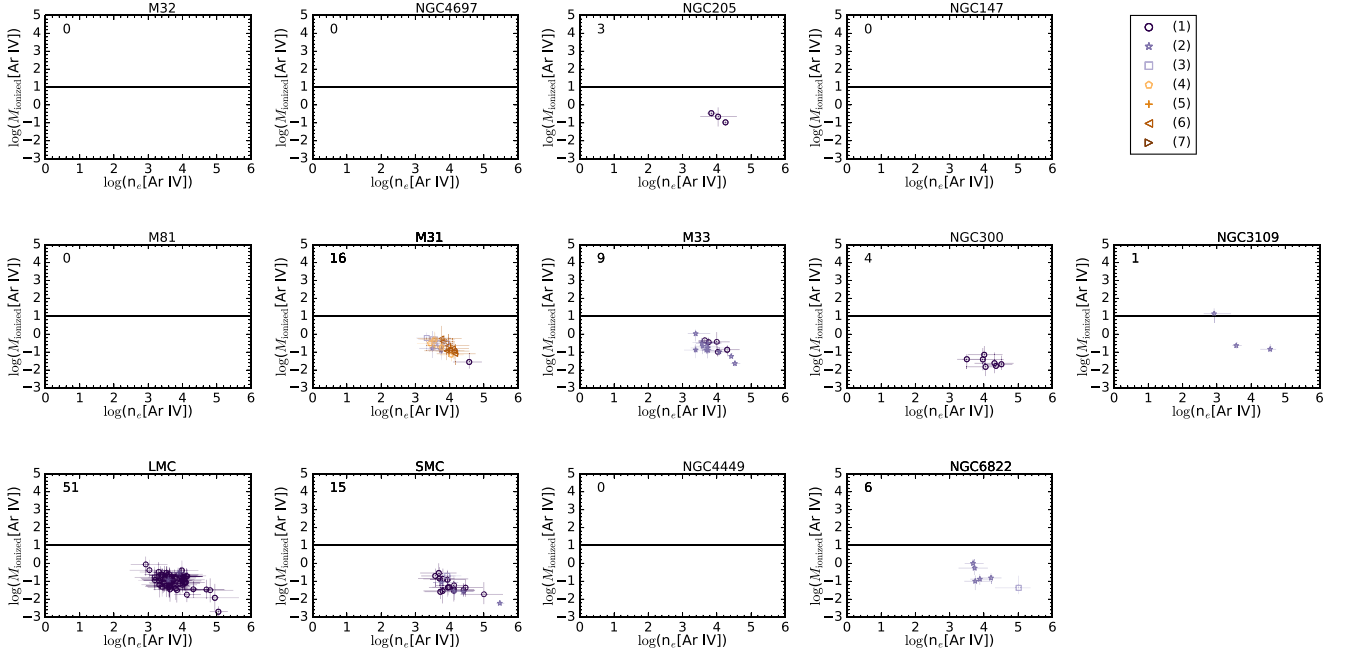
Figure 8. Values of the ionized mass as a function of the electron density derived both from [Ar IV] lines. Upper panels: early-type galaxies, middle panels: spiral galaxies, lower panels: irregular galaxies. The number that appears at the top left corner of each panel indicates the number of PNe plotted in each panel. The numbering of the references is the same as in Fig. 3.

determination of the ionized mass is straightforward if the density is known, and does not depend on the geometry. In equation (1) the density n_e represents some average density of the object, which may not be identical with the one measured by [S II] or [Ar IV] line diagnostics. The densities derived from [S II] and [Ar IV] may actually be higher than the average density of the whole nebula, so the real $M_{ionized}$ may be higher than estimated.

But objects for which the derived nebular mass is larger than, say, 10 M$_\odot$ (this value is marked with a line in the corresponding plots), definitely cannot be PNe. There are some of such objects in NGC 6822 (PN13 and PNS16) and M 33 (PN29, PN30, PN32, PN47, PN48, PN51, PN52, PN59, PN67, PN68, PN90, PN92, and PN94), and it is the case of the majority of objects in M 81 for which the densities were determined (see Fig. 6). The limit of 10 we considered is very conservative. Note also that for those objects, the H β luminosities are higher by one or 2 orders of magnitude than for the rest of our sample (see Fig. 9 to be described later). This indicates that these objects are not PNe and are likely compact H II regions.

For NGC 300, Roth et al. (2018) classified 5 of the 18 objects in common with Peña et al. (2012) as compact H II region candidates and not PNe. They did this on the basis of the high [S II]/Hα ratios observed in these objects, a criterion wrongly attributed to Stasińska et al. (2013). Our determinations of ionized masses suggests that all the objects that Stasińska et al. (2013) considered as are indeed PNe.

In Figs 7 and 8, we see that, in some galaxies, there is an anticorrelation between the ionized masses and the electron densities. This clearly happens for M 31, M 33, M 81, and NGC 300. For a given number of hydrogen ionizing photons, Q_H, the mass of gas that can be ionized is proportional to Q_H/n_e. The behaviour that we see between $M_{ionized}$ suggests that most objects are ionization bounded. This, of course, cannot be considered as fully certain, since we know that the

values of Q_H vary from object to object among PNe, and a deeper analysis is required. However, we note that the objects in the LMC and SMC do not show this trend at all (this is more clearly seen in the plots involving [S II] lines), which suggests that many of them are density-bounded. It is remarkable that such a conclusion has already been reached by Barlow (1987) – though not on the same sample and using different arguments.

Can some of the objects considered in this study be actually SNRs and not PNe? This concern was expressed by Davis et al. (2018). From a diagram plotting [O III]/(Hα + [N II]) versus the absolute magnitude in [O III] λ5007, these authors concluded that SNRs were not likely to contaminate the upper part of the PN luminosity function in M 31 and M 33.

Fig. 9 shows the values of [S II]/Hα as a function of $L_{H\beta}$ for our objects. From a census of optical data on extragalactic SNRs in some of the galaxies of our sample (Long et al. 2010; Leonidaki, Boumis & Zezas 2013; Lee & Lee 2014), SNRs always have [S II]/Hα larger than 0.3 (see Fig. B1 in Appendix B). This implies that objects with [S II]/Hα smaller than 0.3 in our sample cannot be SNRs. Some of our objects do have [S II]/Hα larger than 0.3, but this is not considered incompatible with a PN nature (see fig. 7 of Sabin et al. 2013). On the other hand, SNRs in external galaxies have higher luminosities than PNe. As shown in Fig. B1, five SNRs of 560 have log$L_{H\beta}$ smaller than 2 (and these values are not corrected for extinction, contrary to the values of $L_{H\beta}$ for our samples). The upper right box in Fig. 9 defines the region where SNRs are expected: [S II]/Hα > 0.3 and log$L_{H\beta}$ > 2. As this figure shows, in our samples, we do not see any object in this region (except a few objects in M 81 for which we already know they are not PNe).

We note that the distinction between PNe and other types of nebulae is not necessarily clear-cut from an analysis such as the one we performed here. More information can come from a study of the chemical composition, to be presented in a future paper.
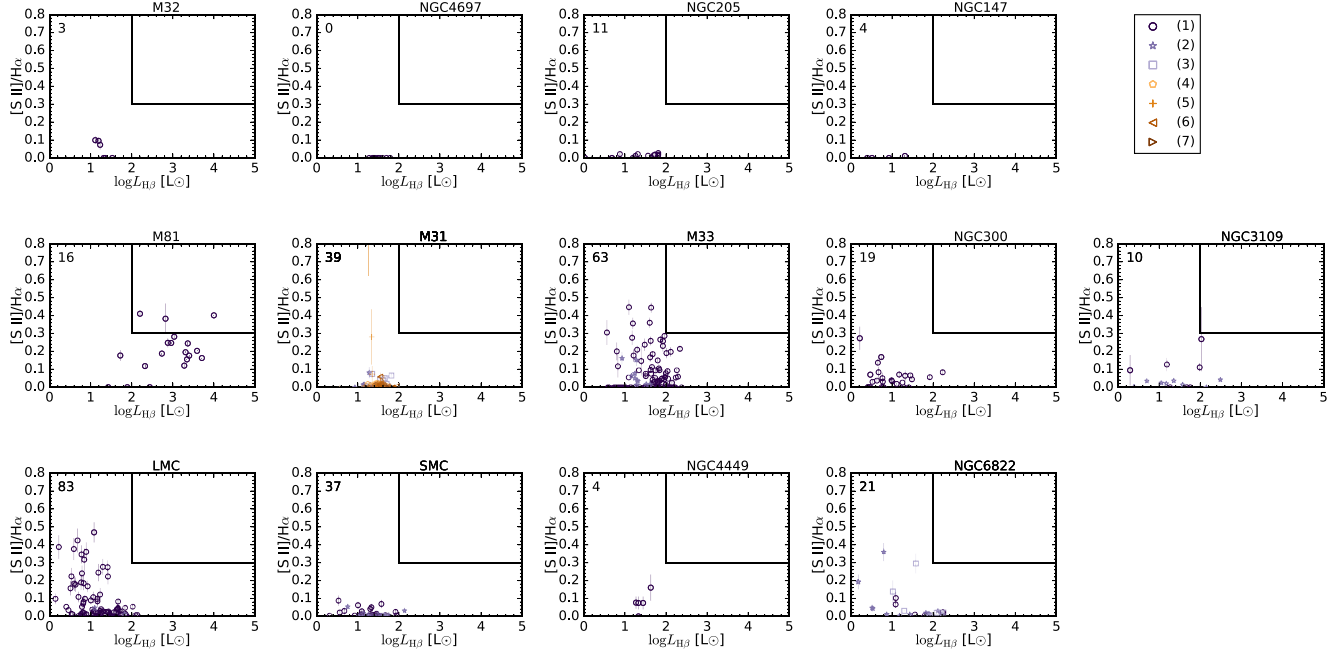
Figure 9. Values of [S II]/Hα as a function of $L_{H\beta}$. Upper panels: early-type galaxies, middle panels: spiral galaxies, lower panels: irregular galaxies. The number that appears at the top left corner of each panel indicates the number of PNe plotted in each panel. The upper right box defines the region where SNRs are expected: [S II]/H$\alpha > 0.3$ and log$(L_{H\beta}) > 2$. The numbering of the references is the same as in Fig. 3.

6 PN EVOLUTION

6.1 Luminosities, densities, and extinction

Figs 10 and 11 show the densities n_e[S II] and n_e[Ar IV] as a function of $L_{H\beta}$. If all the nebulae were to have a similar total mass (including the non-ionized part), one would expect the objects with the lowest densities to correspond to the oldest nebulae. Such an argument is often mentioned in studies of PNe in the Milky Way (Osterbrock & Ferland 2006). It comes naturally from the idea that PNe are expanding. If the brightest PNe were also among the youngest, as is sometimes thought (e.g. Richer 2006) one would expect the densities to be correlated with $L_{H\beta}$. We see this clearly for the LMC and the SMC, but not for the rest of the galaxies. In general there is no correlation, and there even seems to be a slight anticorrelation in M 33. As a matter of fact, $L_{H\beta}$ is not a decreasing function of time. For a given object, as long as it is ionization-bounded, $L_{H\beta}$ is proportional to the rate of variation of the total number of ionizing photons, which, in the first stages of PN evolution first increases an then decreases. As the object becomes density-bounded, $L_{H\beta}$ becomes directly proportional to the density. When considering a collection of objects with different central star masses, as is the case here, the observed plots result from a mixture of time-scales, since more massive central stars evolve more rapidly. In addition, the mass-loss rates at the tip of the AGB as well as the expansion velocities also play a role. A proper interpretation of the behaviour of our samples in the n_e–$L_{H\beta}$ plane therefore requires a modelling approach such as in Stasińska et al. 1998 (a study not taking into account dynamical effects), or, even better, Schönberner et al. 2007 who present a fully hydrodynamical modelling. This will be attempted in forthcoming publications.

Fig. 12 show the value of the extinction $c(H\beta)$ as a function of $L_{H\beta}$. In M 31, M 33, NGC 300, LMC and NGC 6822[3] we see a clear

[3]We exclude M 81 from this consideration, since we have already shown that most – if not all – the objects of the sample are not PNe.

increase of $c(H\beta)$ with increasing $L_{H\beta}$. It has already been argued by Ciardullo & Jacoby (1999), on the basis of observations in M 31, that PNe with progenitors of higher stellar mass have larger extinction. We postpone the question of progenitor masses to a future paper, but we can state that our empirical finding – which appears to be very general – is very important in the context of PN luminosity function studies and their application to the derivation of galaxy distances.

6.2 Evolution of line ratios

Figs 13 and 14 show the variations of He II $\lambda4686$/Hβ and [O III] $\lambda5007$/[O II] $\lambda3727$ as a function of $L_{H\beta}$. These ratios do not depend on abundances (at least directly). The panels have been arranged following the criteria in previous plots, i.e. by increasing order of the de Vaucouleurs index from RC3 (i.e. earliest types on the left top panels, latest types on the right down panels). Different sets of observations for the same galaxy are represented by different colours, as indicated before. The vertical segments represent the error bars. Upper limits are marked by downwards pointing triangles, lower limits by upward-pointing triangles.

One striking aspect of Fig. 13 is the behaviour of He II $\lambda4686$/Hβ in the different samples. This line ratio depends on the effective temperature of the star and on the ionized/neutral nebular mass ratio. It was already noted by Stasińska et al. (1998) that PNe in M 32 and in the bulge of M 31 do not contain objects with high values of He II $\lambda4686$/Hβ, whereas in the LMC there are many objects in which this ratio is much larger that 0.6. This does not mean that the central stars of these objects are more massive and reach higher temperatures, as one might think. As a matter of fact in an ionization bounded nebula, the He II $\lambda4686$/Hβ ratio cannot exceed, say, 0.9, and for stellar temperatures that are lower than 200,000K (which is what is expected for most of PNs according to stellar evolution models, see Bloecker 1995; Miller Bertolami 2016) it is even smaller than 0.6 (see Fig. A1 in the Appendix A). This means that in the LMC and in M 33, and possibly also SMC and NGC 6822, many
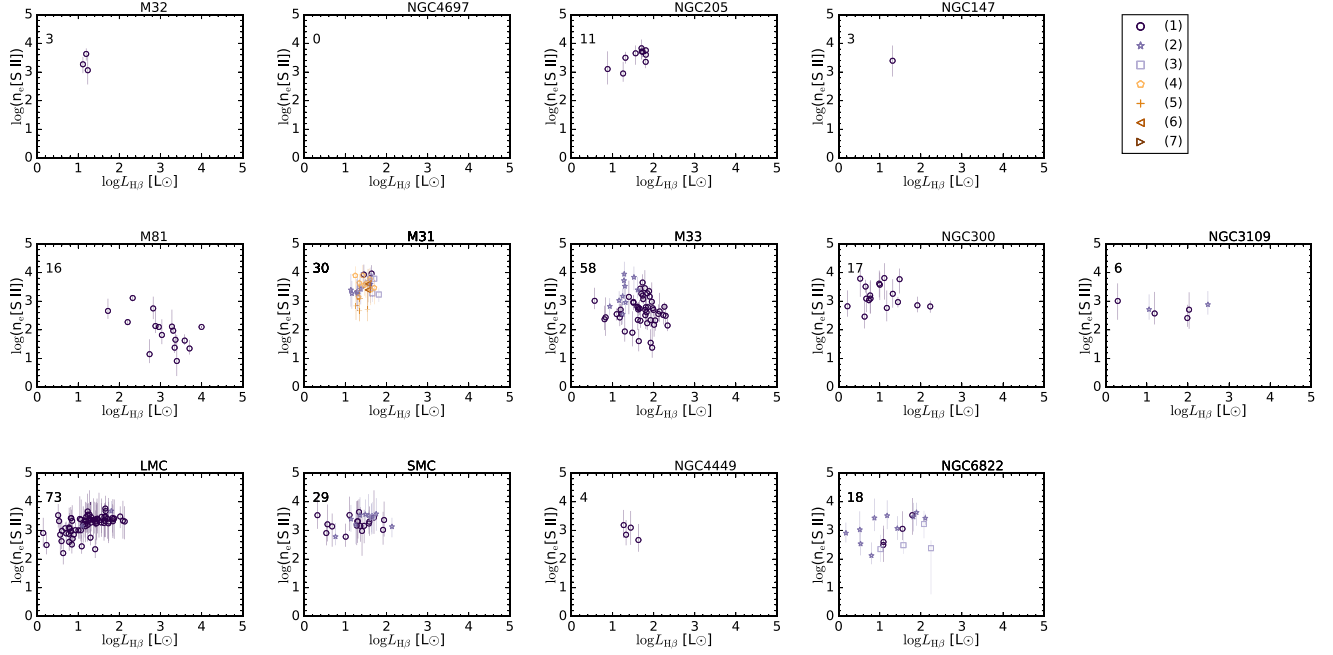
Figure 10. Values of n_e[S II] as a function of $L_{H\beta}$. Upper panels: early-type galaxies, middle panels: spiral galaxies, lower panels: irregular galaxies. The number that appears at the top left corner of each panel indicates the number of PNe plotted in each panel. The numbering of the references is the same as in Fig. 3.
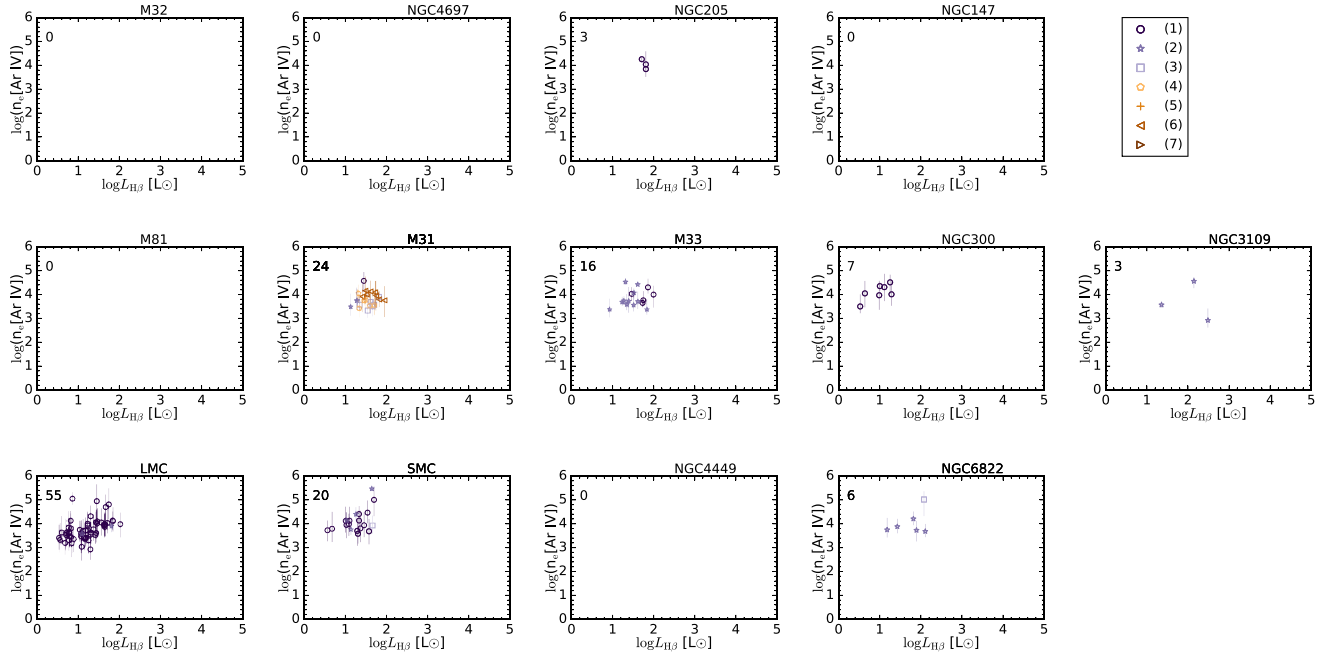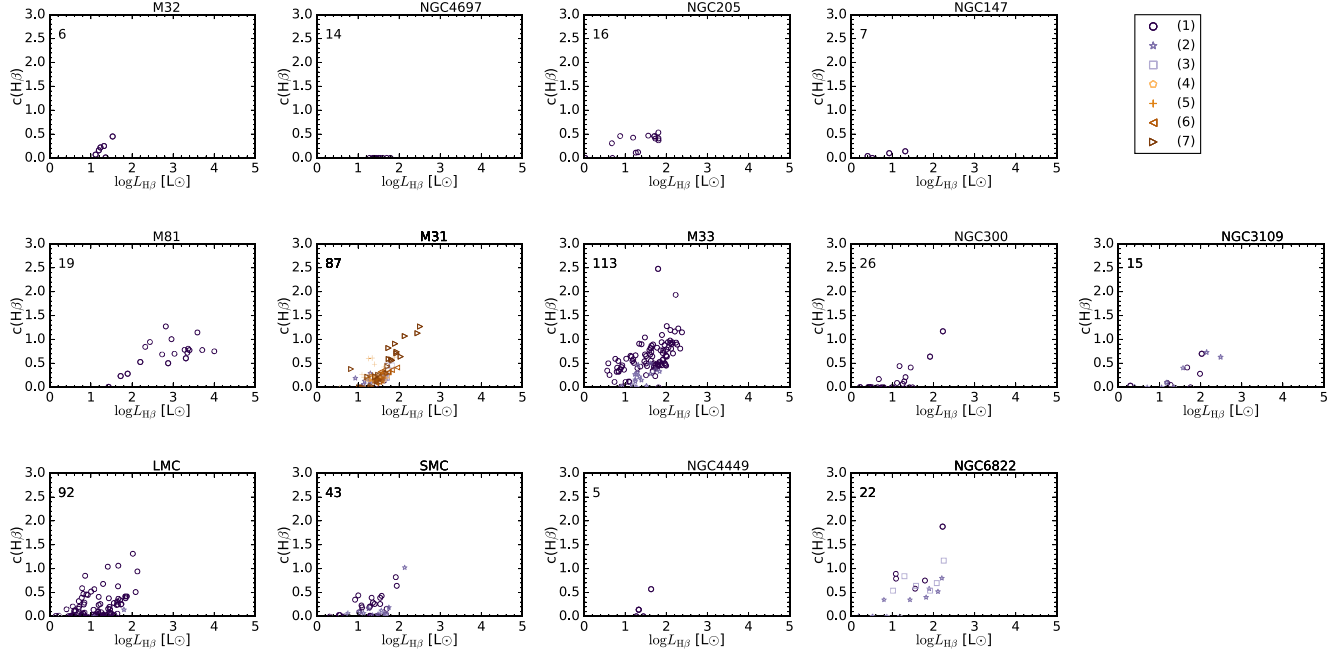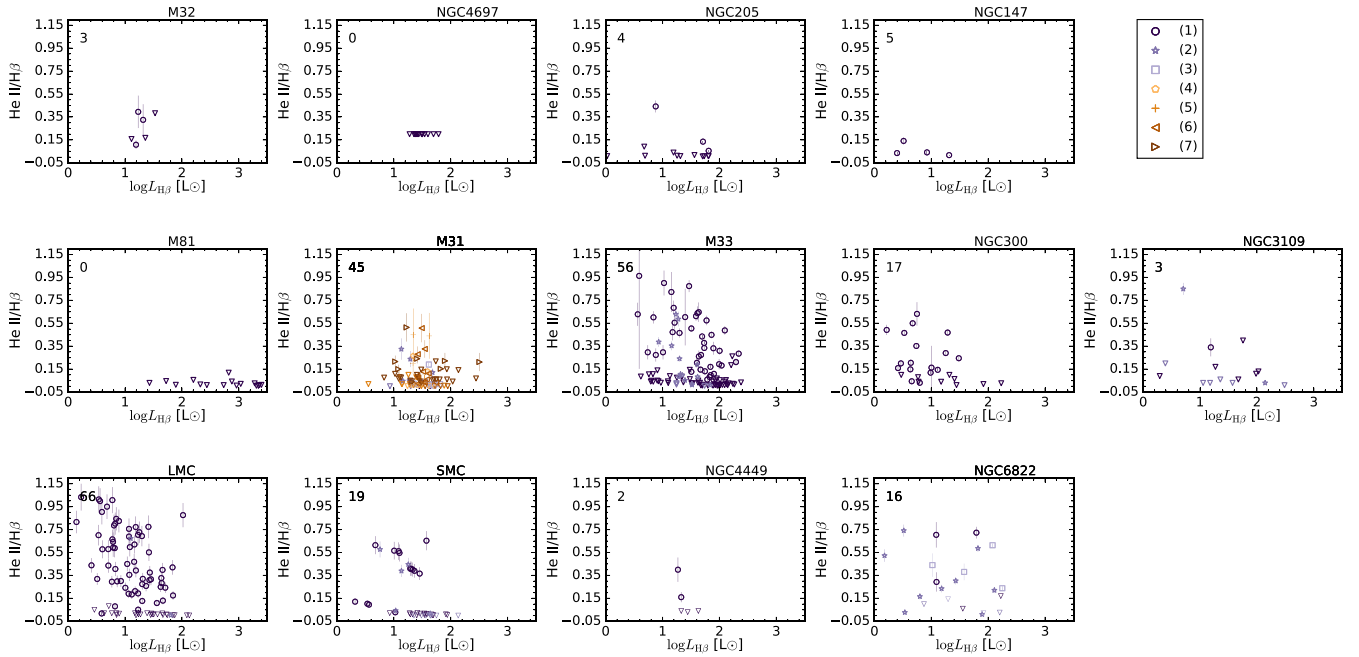

Figure 11. Values of n_e[Ar IV] as a function of $L_{H\beta}$. Upper panels: early-type galaxies, middle panels: spiral galaxies, lower panels: irregular galaxies. The number that appears at the top left corner of each panel indicates the number of PNe plotted in each panel. The numbering of the references is the same as in Fig. 3.

PNe are density bounded. Such a finding strengthens the diagnostic given in Section 5, based on completely different arguments. The reason of this behaviour will be investigated in a future paper. Note that (except in NGC 6822) the highest values of He II λ4686/H β are not found for the PNe with highest H β luminosities. Note also that for M 81, none of the objects has a measured value of He II λ4686, all the upper limits indicate He II λ4686/H β smaller than 0.12. This led Stanghellini et al. (2010) to interpret this fact as due to moderately low central star temperature (less than ∼100 000 K).

A more convincing explanation is that these objects are not PNe but compact H II regions, as argued in the preceding section.

Fig. 14 can be seen as the excitation as a function of H β luminosity. Unfortunately, in many objects of our samples, only a lower limit is available, due to the weakness of [O II] lines. The observations, apart from showing a range of over three decades in [O III] λ5007/[O II] λ3727 do not present any clear trend in most of the panels and do not reveal any strongly different behaviour among the various galaxies. We can just note that the early-type galaxies show consistently the

Figure 12. Values of $c(\mathrm{H}\beta)$ as a function of $L_{\mathrm{H}\beta}$. Upper panels: early-type galaxies, middle panels: spiral galaxies, lower panels: irregular galaxies. The number that appears at the top left corner of each panel indicates the number of PNe plotted in each panel. The numbering of the references is the same as in Fig. 3.

Figure 13. Values of He II $\lambda4686/\mathrm{H}\beta$ as a function of $\log L_{\mathrm{H}\beta}$. Upper panels: early-type galaxies, middle panels: spiral galaxies, lower panels: irregular galaxies. The number that appears at the top left corner of each panel indicates the number of PNe plotted in each panel. The numbering of the references is the same as in Fig. 3.

smallest values of [O III] $\lambda5007$/[O II] $\lambda3727$. Also, in the SMC we do not find such high ratios as in the LMC and M 33, where the PNe with the largest values (or lower limits) of [O III] $\lambda5007$/[O II] $\lambda3727$ are found. The [O III] $\lambda5007$/[O II] $\lambda3727$ intensity ratio depends on many parameters: the effective temperature of the star, the mean ionization parameter, and the ionized/neutral nebular mass ratio. This complex dependence cannot be deciphered without the help of appropriate models. In addition, we must recall that for several samples, a [O III]

$\lambda5007$/H β ratio larger than 3–4 is required for the object to be counted as a PN.

6.3 PN luminosities and the PN luminosity function

So far, in terms of luminosities, we only considered $L_{\mathrm{H}\beta}$, the total luminosity in the H β line, corrected for extinction. The reason is that this is the physical parameter easiest to interpret (see e.g. Dopita,
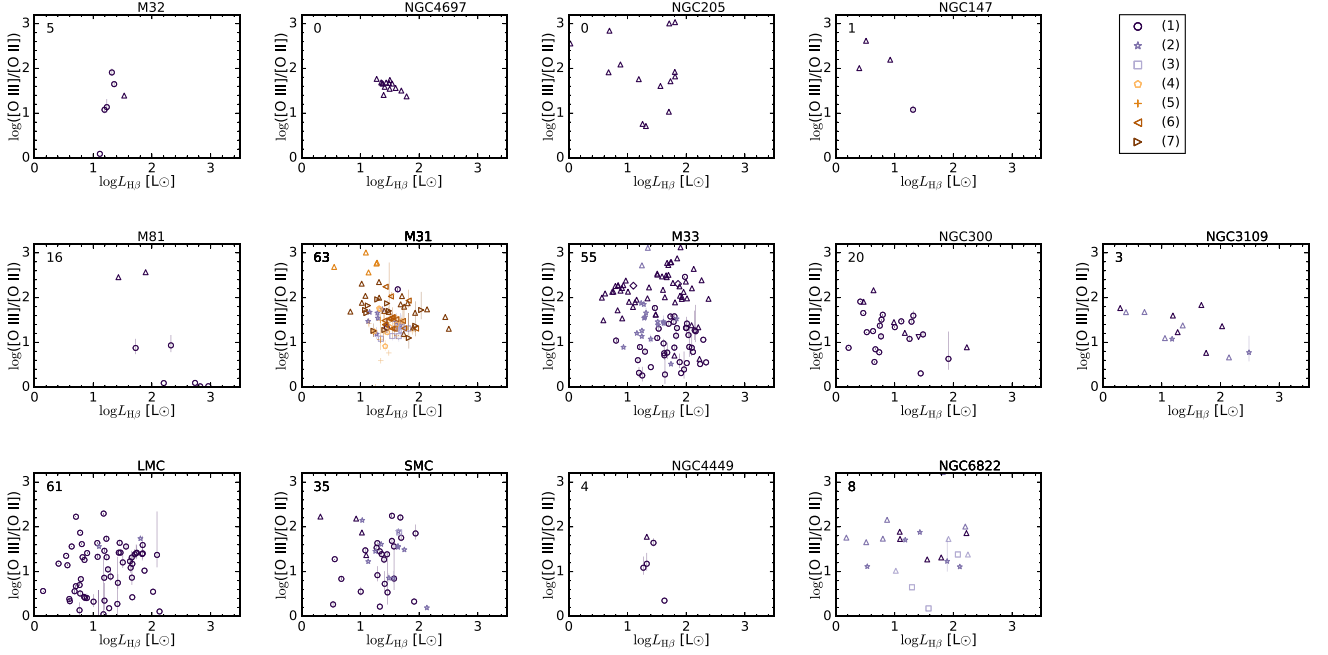
Figure 14. Values of log [O III] λ5007/[O II] λ3727 as a function of log $L_{H\beta}$. Upper panels: early-type galaxies, middle panels: spiral galaxies, lower panels: irregular galaxies. The number that appears at the top left corner of each panel indicates the number of PNe plotted in each panel. The numbering of the references is the same as in Fig. 3.

Jacoby & Vassiliadis 1992; Stanghellini 1995). It depends on the number of ionizing photons emitted by the central star, on the nebular mass and its mean density. We could as well have used $L_{H\alpha}$, which is about three times larger and depends on the same parameters. However, observational studies based on PN luminosities use the observed [O III] magnitudes instead, being [O III] λ5007 the brightest line in such objects. Actually, the detection of extragalactic PNe mainly relies on [O III]. Many studies of the PNLF concluded that the bright end cut-off luminosity of the PNLF is invariant with respect to galaxy type and position in the galaxy, allowing the use of the PNLF as a tool to measure galaxy distances (see Ciardullo 2016, for a recent review). As expressed in that paper, it is not yet clear why this technique works so well, because the observed [O III] luminosity, $L_{[O III]}^{obs}$, also depends on metallicity, excitation and reddening.

In Figs 15 and 16, we show the relation between the logarithms of the [O III] and H β luminosities, corrected and uncorrected for extinction, respectively. In both figures, the thin line represents the one-to-one relation. The thick solid line and the dashed lines are obtained from the mean and the standard deviation of $L_{[O III]}/L_{H\beta}$.

Figs 15 and 16 show that, for most PNe of our samples, the relation $L_{[O III]}/L_{H\beta} = 10 \pm 5$ holds. Only about 14 per cent of the PNe have $L_{[O III]}^{corr}/L_{H\beta}^{corr}$ below 5. Those are objects of lower excitation than the majority and they can be found at any value of $L_{H\beta}^{corr}$ in the diagrams, even at the highest ones (e.g. in NGC 3109 or the LMC). This, a priori, could affect the [O III] PNLF and its use for distances. As mentioned before, our samples are probably biased against such objects. In some galaxies (M 32, NGC 4697, M 31), the majority of the PNe are slightly above the thick line, while in the SMC and NGC 6822, they are slightly below. This is likely related to the metallicity, and will be studied in more detail in forthcoming papers.

In Fig. 16, the objects are displaced along the diagonal to the left with respect to their position in Fig. 15 because the values of $f(\lambda)$ are very similar for [O III] and H β. Since, as seen in Fig. 12, the extinction tends to be larger for larger values of $L_{H\beta}$, the points in

Fig. 16 are less spread along the diagonal direction than in Fig. 15. In Fig. 16, the values of the observed [O III] luminosities, log $L_{[O III]}^{obs}$, correspond to those used in PNLF studies. Most galaxies have their upper values of log $L_{[O III]}^{obs}$ at 2.54 ± 0.25, with a few exceptions (NGC 3109, NGC 147). Note that, although spectroscopic studies have been made on bright PNe, PNLF samples may contain a larger number of bright PNe than those reported here, so that the luminosity distribution of the PNe of our samples is not necessarily identical with the PNLF derived from photometric observations of large samples of PNe. Note also that the distances used in this paper are those recommended by Jarrett et al. (2019) based on an analysis of several distance indicators, and, in some cases, are somewhat distinct from the PNLF distances.

7 CONCLUSIONS

With the aim of a comparative study of the PN populations in different galaxies, we have collected a sample of published spectroscopic data on 470 objects in 13 galaxies. The data were selected according to various requirements so that the final sample is as homogeneous as possible. The star formation histories and morphological types of the galaxies used here cover a wide range and thus, their PN progenitor stars are expected to have different masses.

We are aware that the samples of PNe studied here are not complete. An adequate analysis of the populations of PNe in external galaxies requires to have data of all the PNe located in a particular field of each of these galaxies. We also want to highlight that by summarizing all the available observations of extragalactic PNe that fall within a set of selection criteria; we were able to obtain some interesting findings, even though the samples are not complete or homogeneous.

The emission lines compiled are 28 but in this paper we studied only a few of them. The others will be used in a future paper to study chemical abundances. If upper limits of [O II] λ3727,
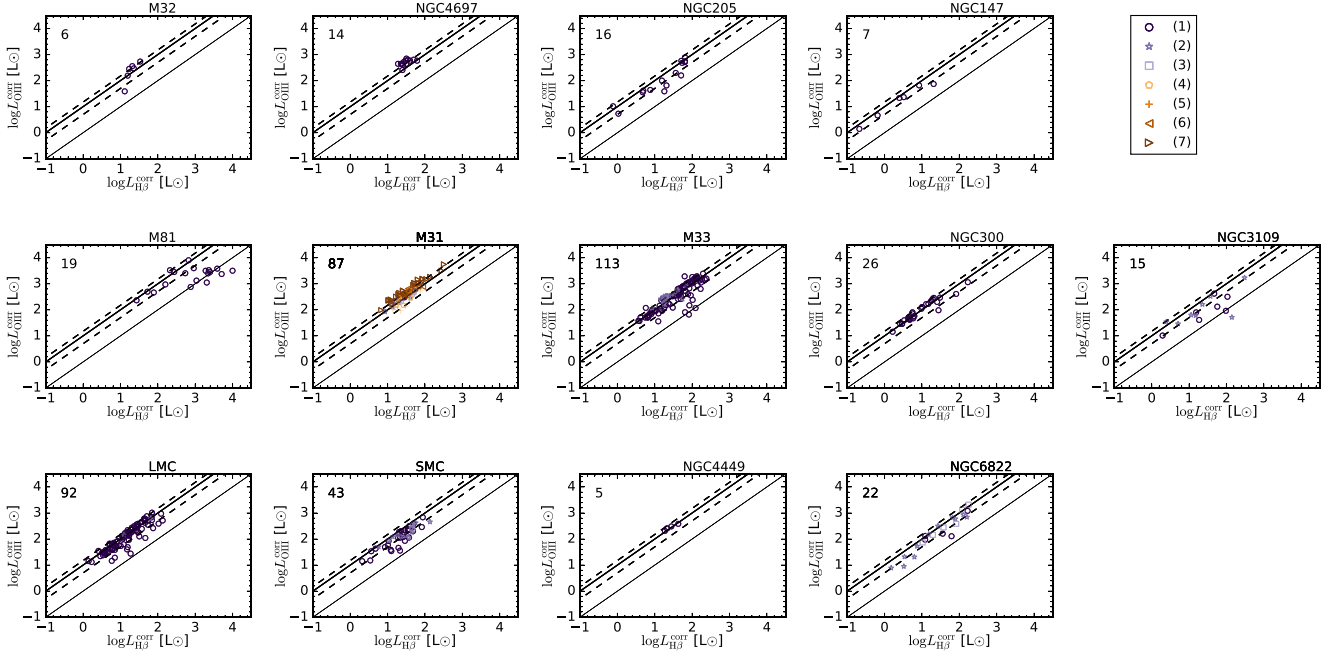
Figure 15. Values of log $L^{corr}_{[O\,III]}$ as a function of log $L^{corr}_{H\beta}$. Upper panels: early-type galaxies, middle panels: spiral galaxies, lower panels: irregular galaxies. The number that appears at the top left corner of each panel indicates the number of PNe plotted in each panel. The thin line represents where $L^{corr}_{[O\,III]} = L^{corr}_{H\beta}$, whereas the thick solid line and the dashed lines are obtained from the mean and the standard deviation of $L^{corr}_{[O\,III]}/L^{corr}_{H\beta}$. The numbering of the references is the same as in Fig. 3.
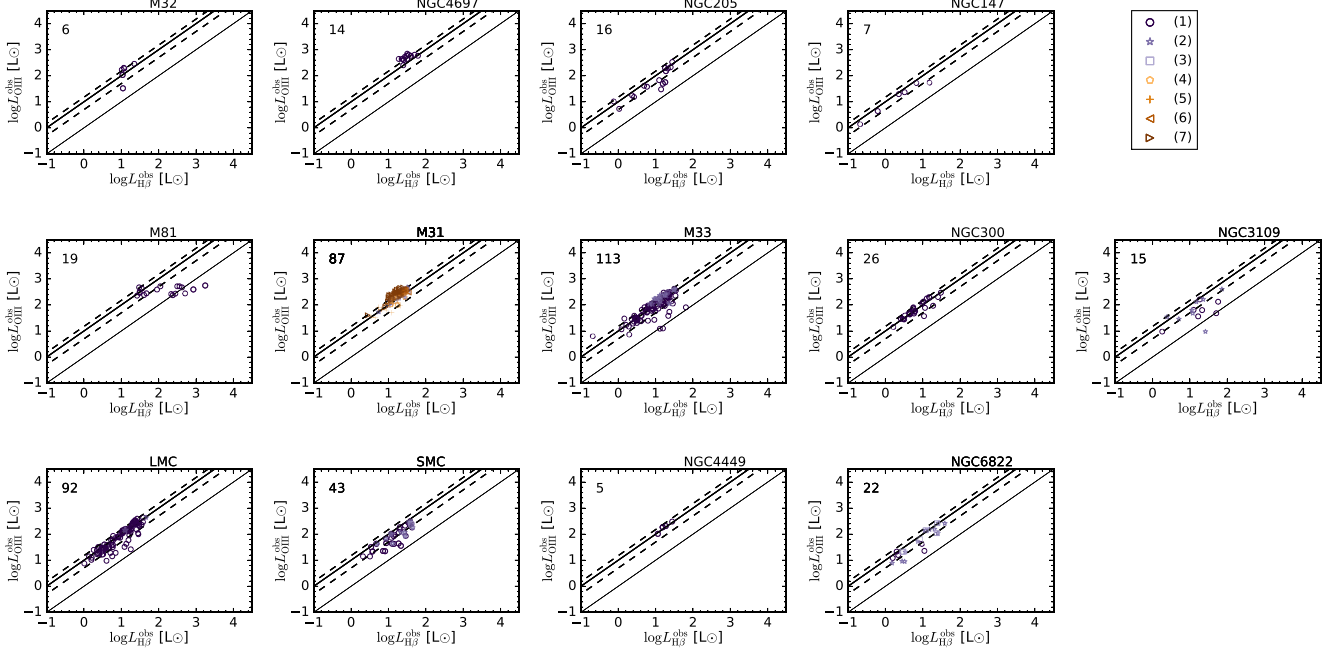
Figure 16. Values of log $L^{obs}_{[O\,III]}$ as a function of log $L^{obs}_{H\beta}$. Upper panels: early-type galaxies, middle panels: spiral galaxies, lower panels: irregular galaxies. The number that appears at the top left corner of each panel indicates the number of PNe plotted in each panel. The thin line represents where $L^{obs}_{[O\,III]} = L^{obs}_{H\beta}$; the thick solid line and the dashed lines are obtained from the mean and the standard deviation of $L^{obs}_{[O\,III]}/L^{obs}_{H\beta}$. The numbering of the references is the same as in Fig. 3.

[O III] λ5007, He I λ5876, and He II λ4686 are not provided by the authors, we have adopted as an upper limit the uncertainty of a nearby and weak line. A few references do not provide uncertainties for the line fluxes and we estimated them from a logarithmic linear fit to the relative uncertainties versus line fluxes from other observations with similar characteristics. We have also compiled the available [O III] λ5007 magnitudes to derive [O III] luminosities. If the magnitudes were not available we have used the spectroscopic data to compute the luminosities. The comparison between the theoretical and observed values of the [N II] λ6584/λ6548, [O III] λ5007/λ4959, and H γ/H β ratios allow us to find out if the uncertainties were adequately estimated, if there could be spectral calibration prob-

lems, or if the stellar absorption has not been taken into account correctly.

We have studied the electron densities derived from [S II] and [Ar IV] lines. Most of the PNe have densities in the range 1 000–10 000 cm^{-3}. In the sample studied here there is a general tendency for the [Ar IV] density to be higher than the [S II] density, in some cases by a large factor. This result is in contradiction with recent findings by Rodríguez (2020) in Galactic PNe. The fact that the observed portion in Galactic are generally much smaller than the entire objects could perhaps explain the difference, but this hypothesis needs testing.

A crucial aspect in the study of extragalactic PNe is the discrimination between PNe and other objects such as H II regions and SNR. We have explored several diagnostics that help us to identify PNe. The ionized masses and Hβ luminosities reveal that around 30 objects identified as PNe in previous papers are likely compact H II regions. In particular this concerns most of the objects in M 81 in the sample of Stanghellini et al. (2010). On the other hand, we found that the five objects from Peña et al. (2012) classified as compact H II regions by Roth et al. (2018) are actually PNe. From the analysis of the values of [S II]/Hα and Hβ luminosities, we concluded that there are not SNRs in our sample.

We found a clear anticorrelation between the ionized masses and the electron densities in M 31, M 33, and NGC 300 that suggests that most of the PNe are ionization bounded. This trend is completely absent in LMC and SMC that could be indicating that many of the PNe observed in these galaxies are density bounded.

We found no correlation between the electron densities and the Hβ luminosities that indicates that the brightest PNe are not necessarily the youngest. An increase of c(Hβ) with the Hβ luminosities is found in M 31, M 33, NGC 300, LMC, and NGC 6822 that can be caused by a higher amount of dust in more massive progenitor stars as suggested by Ciardullo & Jacoby (1999). These two results that are related to the progenitor masses will be studied in a future paper.

Finally, we have studied the correlations between He II λ4686/Hβ, log [O III] λ5007/[O II] λ3727, and $L_{\text{H}\beta}$ that are not directly dependent on abundances. The PNe in LMC, M 33, and possibly SMC have higher values of He II λ4686/Hβ than the PNe in other galaxies. According to photoionization models, this indicates that many PNe in LMC and some in M 33 and SMC are density bounded, in agreement with the behaviour of the ionized masses with respect to the electron densities. The PNe studied here cover a wide range in the [O III] λ5007/[O II] λ3727 values being M 33 the galaxy where the highest values are found and the early-type galaxies those with the lowest values.

As for the $L_{\text{H}\beta}-L_{\text{[O III]}}$ relation, we found that they are strongly correlated. This means that the upper limit of the PNLF based on [O III] magnitudes and used as a means to measure galaxy distances, can be investigated by first analyzing Hβ(or Hα) luminosities, which are much easier to interpret in terms of the the populations of PN progenitors. The difference between $L_{\text{H}\beta}-L_{\text{[O III]}}$ is a second-order effect on the [O III] PNLF, which can be studied in a second step.

In conclusion, the relatively simple analysis performed here from a few intensity ratios and parameters derived from these intensity ratios allows us to obtain some first findings. First, we show that there are a few parameters that are essential to distinguish PNe from other related objects: the ionized mass and the $L_{\text{H}\beta}$ to discriminate between PNe and compact H II regions and the [S II]/Hα and the $L_{\text{H}\beta}$ to identify SNRs. Secondly, we found some indications that the PNe (and their progenitors) are different in the different galaxies: (1) most of the PNe in the spiral galaxies M 31, M 33, and NGC 300 seem to be ionization bounded, whereas many of those in the irregular galaxies

LMC and SMC are likely density bounded, (2) The extinction appears to be correlated with the intrinsic luminosity, which is an important clue for the study of the PN luminosity function based on [O III] magnitudes. Further papers of this series will analyse topics related the PN progenitors and their evolution as well as topics related to their chemical composition.

DATA AVAILABILITY

This paper use data compiled from published sources whose references are given in the text. The whole compilation will be made publicly available when all the papers of the series are published.

REFERENCES

Annibali F. et al., 2017, ApJ, 843, 20
Asplund M., Grevesse N., Sauval A. J., Scott P., 2009, ARA&A, 47, 481
Bacon R. et al., 2010, in McLean I. S., Ramsay S. K., Takami H., eds, Proc. SPIE Conf. Ser. Vol. 7735, Ground-based and Airborne Instrumentation for Astronomy III. SPIE, Bellingham, p. 773508
Balick B., Kwitter K. B., Corradi R. L. M., Henry R. B. C., 2013, ApJ, 774, 3
Barlow M. J., 1987, MNRAS, 227, 161
Bloecker T., 1995, A&A, 299, 755
Bresolin F., Stasińska G., Vílchez J. M., Simon J. D., Rosolowsky E., 2010, MNRAS, 404, 1679
Cardelli J. A., Clayton G. C., Mathis J. S., 1989, ApJ, 345, 245
Chornay N., Walton N. A., 2020, A&A , 638, A103
Ciardullo R., 2016, Proc. IAU Symp. 29B, Astronomy in Focus. IAU XXIX General Assembly, 2015. Cambridge Univ. Press, Cambridge, p. 15
Ciardullo R., Jacoby G. H., 1999, ApJ, 515, 191
Ciardullo R., Jacoby G. H., Ford H. C., Neill J. D., 1989, ApJ, 339, 53
Ciardullo R., Durrell P. R., Laychak M. B., Herrmann K. A., Moody K., Jacoby G. H., Feldmeier J. J., 2004, ApJ, 614, 167

Corradi R. L. M. et al., 2005, A&A, 431, 555

Corradi R. L. M., Kwitter K. B., Balick B., Henry R. B. C., Hensley K., 2015, ApJ, 807, 181

Davis B. D., Ciardullo R., Feldmeier J. J., Jacoby G. H., 2018, Res. Notes Am. Astron. Soc., 2, 32

de Vaucouleurs G., de Vaucouleurs A., Corwin Herold G. J., Buta R. J., Paturel G., Fouque P., 1991, Third Reference Catalogue of Bright Galaxies. Springer, New York

Dopita M. A., Jacoby G. H., Vassiliadis E., 1992, ApJ, 389, 27

Fang X., García-Benito R., Guerrero M. A., Liu X., Yuan H., Zhang Y., Zhang B., 2015, ApJ, 815, 69

Fang X. et al., 2018, ApJ, 853, 50

Ferland G. J. et al., 2017, Rev. Mex. Astron. Astrofís., 53, 385

Flores-Durán S. N., Peña M., Ruiz M. T., 2017, A&A, 601, A147

Froese Fischer C., Tachiev G., 2004, At. Data Nucl. Data Tables, 87, 1

García-Rojas J., Peña M., Flores-Durán S., Hernández-Martínez L., 2016, A&A, 586, A59

Gesicki K., Zijlstra A. A., Hajduk M., Szyszka C., 2014, A&A, 566, A48

González-Santamaría I., Manteiga M., Manchado A., Ulla A., Dafonte C., 2019, A&A, 630, A150

Gonçalves D. R., Magrini L., Leisy P., Corradi R. L. M., 2007, MNRAS, 375, 715

Gonçalves D. R., Magrini L., Martins L. P., Teodorescu A. M., Quireza C., 2012, MNRAS, 419, 854

Gonçalves D. R., Magrini L., Teodorescu A. M., Carneiro C. M., 2014, MNRAS, 444, 1705

Górny S. K., Stasińska G., Escudero A. V., Costa R. D. D., 2004, A&A, 427, 231

Górny S. K., Chiappini C., Stasińska G., Cuisinier F., 2009, A&A, 500, 1089

Hernández-Martínez L., Peña M., Carigi L., García-Rojas J., 2009, A&A, 505, 1027

Jacoby G. H., 1989, ApJ, 339, 39

Jacoby G. H., Ciardullo R., 1999, ApJ, 515, 169

Jacoby G. H., Walker A. R., Ciardullo R., 1990, ApJ, 365, 471

Jarrett T. H., Cluver M. E., Brown M. J. I., Dale D. A., Tsai C. W., Masci F., 2019, ApJS, 245, 25

Kimeswenger S., Barría D., 2018, A&A, 616, L2

Kreckel K., Groves B., Bigiel F., Blanc G. A., Kruijssen J. M. D., Hughes A., Schruba A., Schinnerer E., 2017, ApJ, 834, 174

Kwitter K. B., Lehman E. M. M., Balick B., Henry R. B. C., 2012, ApJ, 753, 12

Lee J. H., Lee M. G., 2014, ApJ, 786, 130

Leisy P., Corradi R. L. M., Magrini L., Greimel R., Mampaso A., Dennefeld M., 2005, A&A, 436, 437

Leisy P., Dennefeld M., 2006, A&A, 456, 451

Leonidaki I., Boumis P., Zezas A., 2013, MNRAS, 429, 189

Long K. S. et al., 2010, ApJS, 187, 495

Luridiana V., Morisset C., Shaw R. A., 2015, A&A, 573, A42

Magrini L., Gonçalves D. R., 2009, MNRAS, 398, 280

Magrini L., Corradi R. L. M., Mampaso A., Perinotto M., 2000, A&A, 355, 713

Magrini L., Perinotto M., Corradi R. L. M., Mampaso A., 2001, A&A, 379, 90

Magrini L., Leisy P., Corradi R. L. M., Perinotto M., Mampaso A., Vílchez J. M., 2005, A&A, 443, 115

Magrini L., Stanghellini L., Villaver E., 2009, ApJ, 696, 729

Mendoza C., Zeippen C. J., 1982, MNRAS, 198, 127

Merrett H. R. et al., 2006, MNRAS, 369, 120

Miller Bertolami M. M., 2016, A&A, 588, A25

Morisset C., 2013, in pyCloudy: Tools to Manage Astronomical Cloudy Photoionization Code, record ascl:1304.020

Morisset C., 2014, in Morisset C., Delgado-Inglada G., Torres-Peimbert S., eds, Proc. Conf., Asymmetrical Planetary Nebulae VI Conference. p. 62

Méndez R. H., 2017, in Liu X., Stanghellini L., Karakas A., eds, Proc. IAU Symp. 323, Planetary Nebulae: Multi-Wavelength Probes of Stellar and Galactic Evolution. Kluwer, Dordrecht, p. 298

Méndez R. H., Riffeser A., Kudritzki R. P., Matthias M., Freeman K. C., Arnaboldi M., Capaccioli M., Gerhard O. E., 2001, ApJ, 563, 135

Méndez R. H., Thomas D., Saglia R. P., Maraston C., Kudritzki R. P., Bender R., 2005, ApJ, 627, 767

Osterbrock D. E., Ferland G. J., 2006, Astrophysics of Gaseous Nebulae and Active Galactic Nuclei, 2nd edn. University Science Books, Sausalito, CA

Paczyński B., 1971, Acta Astron., 21, 417

Peña M., Richer M. G., Stasińska G., 2007a, A&A, 466, 75

Peña M., Stasińska G., Richer M. G., 2007b, A&A, 476, 745

Peña M., Reyes-Pérez J., Hernández-Martínez L., Pérez-Guillén M., 2012, A&A, 547, A78

Porter R. L., Ferland G. J., Storey P. J., Detisch M. J., 2012, MNRAS, 425, L28

Porter R. L., Ferland G. J., Storey P. J., Detisch M. J., 2013, MNRAS, 433, L89

Ramsbottom C. A., Bell K. L., 1997, At. Data Nucl. Data Tables, 66, 65

Richard J. et al., 2019, preprint (arXiv:1906.01657)

Richer M. G., 1993, ApJ, 415, 240

Richer M. G., 2006, in Barlow M. J., Méndez R. H., eds, Proc. IAU Symp. 234, Planetary Nebulae in our Galaxy and Beyond. Kluwer, Dordrecht, p. 317

Richer M. G., 2011, in Henney W. J., Torres-Peimbert S., eds, XIII Latin American Regional IAU Meeting, Vol. 40, Revista Mexicana de Astronomía y Astrofísica (Serie de Conferencias). p. 251

Richer M. G., McCall M. L., 2007, ApJ, 658, 328

Richer M. G., McCall M. L., 2016, in Bragaglia A., Arnaboldi M., Rejkuba M., Romano D., eds, Proc. IAU Symp. 317, The General Assembly of Galaxy Halos: Structure, Origin and Evolution. Kluwer, Dordrecht, p. 344

Richer M. G., Stasińska G., McCall M. L., 1999, A&AS, 135, 203

Rodríguez M., 2020, MNRAS, 495, 1016

Roth M. M., Becker T., Kelz A., Schmoll J., 2004, ApJ, 603, 531

Roth M. M. et al., 2018, A&A, 618, A3

Sabin L. et al., 2013, MNRAS, 431, 279

Schlafly E. F., Finkbeiner D. P., 2011, ApJ, 737, 103

Schoenberner D., 1983, ApJ, 272, 708

Schönberner D., Jacob R., Steffen M., Sandin C., 2007, A&A, 473, 467

Shaw R. A. et al., 2010, ApJ, 717, 562

Soffner T., Mendez R. H., Jacoby G. H., Ciardullo R., Roth M. M., Kudritzki R. P., 1996, A&A, 306, 9

Stanghellini L., 1995, ApJ, 452, 515

Stanghellini L., Shaw R. A., Balick B., Mutchler M., Blades J. C., Villaver E., 2003, ApJ, 596, 997

Stanghellini L., Magrini L., Villaver E., Galli D., 2010, A&A, 521, A3

Stanghellini L., Bucciarelli B., Lattanzi M. G., Morbidelli R., 2020, ApJ, 889, 21

Stasińska G., Tylenda R., 1986, A&A, 155, 137

Stasińska G., Richer M. G., McCall M. L., 1998, A&A, 336, 667

Stasińska G., Peña M., Bresolin F., Tsamis Y. G., 2013, A&A, 552, A12

Storey P. J., Hummer D. G., 1995, MNRAS, 272, 41

Storey P. J., Zeippen C. J., 2000, MNRAS, 312, 813

Storey P. J., Sochi T., Badnell N. R., 2014, MNRAS, 441, 3028

Tayal S. S., Zatsarinny O., 2010, ApJS, 188, 32

Tsamis Y. G., Barlow M. J., Liu X. W., Danziger I. J., Storey P. J., 2003, MNRAS, 345, 186

Tufte E. R., 1990, Unvisioning Information. Graphics Press, Cheshire

Valenzuela L. M., Méndez R. H., Miller Bertolami M. M., 2019, ApJ, 887, 65

Vassiliadis E., Wood P. R., 1993, ApJ, 413, 641

Walsh J. R., Rejkuba M., Walton N. A., 2015, A&A, 574, A109

Webster B. L., 1976, MNRAS, 174, 513

Wright E. L. et al., 2010, AJ, 140, 1868

APPENDIX A: MAXIMUM VALUES OF HE II/H β IN PNE

Under the condition that the nebular gas absorbs all the ionizing photons from the central star, the ratio He II/H β is an indicator of the
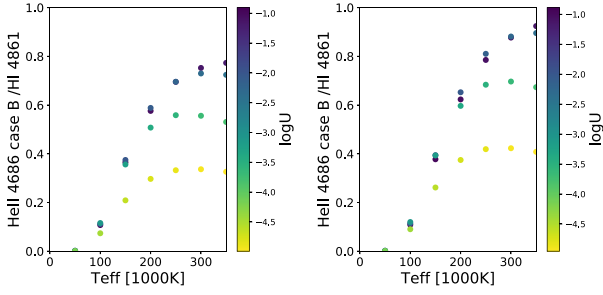
Figure A1. Values of He II/H β as a function of the effective temperature for a sample of photoionization models. Left-hand panel: He/H = 0.10, right-hand panel He/H = 0.15. The colour bar runs from low to high ionization parameter values.

effective temperature. However, as shown by Stasińska & Tylenda (1986), the He II/H β ratio also depends on the ionization parameter. The reason is that not all photons with energies above 54.4 eV are absorbed by He$^+$, some are absorbed by neutral hydrogen atoms, whose abundance with respect to He$^+$ increases in the He^{++} zone as the ionization parameter decreases. In addition, the He II/H β ratio levels off at temperatures above 250–350 kK because the proportion of He$^+$ ionizing photons emitted by the star increases more slowly with temperature.

To illustrate this and find the maximum value of He II/H β expected in ionization bounded PNe, we have computed two sequences of ionization bounded models using CLOUDY (Ferland et al. 2017) version 17.01 and PyCLOUDY (Morisset 2013, 2014). The exciting star is a blackbody, with effective temperature going from 50 000 to 350 000 K, the log of the mean ionization parameter, <U>, ranges from −4 to −2, the electron density is 10^3 cm^{-3}, and the geometry is a filled sphere. The abundances of the heavy elements are the solar photospheric ones from Asplund et al. (2009).

Fig. A1 shows the resulting values of He II (case B)/H β as a function of the effective temperature for the computed models.[4] In

---

[4]We plot the case B values because our models considered a small number of n-resolved levels, and case B gives an upper limit to the real He II λ4686 emissivities.

the left-hand panel, the models have He/H = 0.10, in the right one they have He/H = 0.15. We see that the maximum value of He II/H β reached by the models is ∼0.9.

However, according to the evolution models for post-AGB stars by Miller Bertolami (2016), the effective temperature exceeds 250 kK only for the most massive stars and for a very short time, so such cases are expected to be rare.

APPENDIX B: DISTINGUISHING PLANETARY NEBULAE FROM SUPERNOVA REMNANTS

We have compiled the values of S II/H α and H α luminosities for SNRs in M 31, M 33, and NGC 4449 from Lee & Lee (2014), Long et al. (2010), and Leonidaki et al. (2013), respectively. The values are plotted in Fig. B1. The lower value of S II/H α in this sample of SNR is ∼0.3. On the other hand, $\log L_{H\beta} \sim 2$ can be taken as the lower value of the H β luminosity since only 5 of 560 SNRs are below this limit.
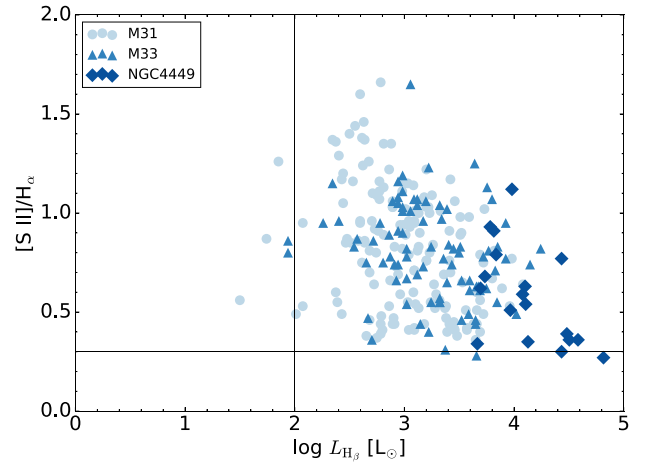
Figure B1. Values of [S II]/H α as a function of $\log L_{H\beta}$ for supernova remnants in M 31, M 33, and NGC 4449.

This paper has been typeset from a TEX/LATEX file prepared by the author.